University of Zurich[UZH]

Observations of virga precipitation with a Micro Rain Radar

Master-Thesis

Author:
Ruben Beynon

Supervisor:
Klemens Hocke

Date:
December 17, 2021

Contents

Abstract

Studies of snow virga precipitation are rare, the only description of it known to us being by Jullien et al. [13]. In this study, we investigated data from a Micro-Rain Radar (MRR) in Bern, Switzerland, from 2008 to 2013 for snow virga precipitation events. The MRR data were reprocessed with the radar data processing by Garcia-Benardi et al. [6] which allows the detection of snow virga precipitation. From the events we found, we have selected two which we present. The reviews of the events are additionally supported by atmospheric reanalysis data and atmospheric back trajectories. In the investigated events, we were in both cases able to observe a wind shear during the snow virga precipitation. While the wind shear existed, the situation was in both cases that moist and precipitating air was in the upper air layers while dry air was carried into the lower air layers.

Introduction

Observing precipitation supports its understanding and thus contributes to the exploration of the atmosphere and its mechanics, which, as the habitat of humankind, is of central importance to society that affects large areas of everyday life. This work presents and investigates two cases of virga precipitation, recorded by a vertically aligned K-band Doppler radar in Bern, Switzerland. To investigate the cases, the work combines Doppler radar data with atmospheric reanalysis data and atmospheric back trajectories.
The Doppler radar data set examined as the basis for the investigations covers measurements over the years from 2008 to 2013. In a first part, these were checked for their temporal completeness and, in the further course, for their accuracy and credibility by comparing them against other meteorological measuring devices. This revealed both weaknesses in the measurements as well as malfunctions of the radar. However, this enabled one to get an impression of its reliability as well as an understanding of its possibilities and limitations.
Afterwards, the data was revised in order to increase its accuracy and to obtain further information from it. In the process, a data retrieval was implemented which automatically revises the newly collected data from the radar that is currently still in operation. In the revised data, a search was performed for virga or virga-like events and a selection was made for particularly suitable cases in terms of their duration and characteristics. For the two cases which were chosen, the corresponding reanalysis data has been edited and the back trajectories were generated in order to have a more comprehensive picture.

CHAPTER 1

Principle of Radar

As an introduction to weather radars, we first discuss the radar equation, which establishes a relationship between transmitting and receiving power, as well as the radar reflectivity factor, a parameter that is almost the most important in weather radar theory.

1.1 Radar Equation

To deduce the radar equation, consider a wave scattered by a single backscatterer and that the wave is transmitted and received by the same radar antenna. At the location of the target, at a height h over the antenna, the intensity of the incident wave S_t is proportional to one over distance squared and linearly dependent on the transmit power of the antenna P_t, assuming an isotropically radiating antenna.

$$S_t = g\frac{P_t}{4\pi h^2} \tag{1.1}$$

To correct for the anisotropic nature of the antenna, the antenna gain g is introduced, which is the gain of the transmitting antenna in the direction of the target. For simplicity, it is assumed to be a constant factor for the further calculations.

The intensity scattered by the target is the product of the incident intensity S_t and the cross section σ of the target. From this, the incident intensity at the location of the receiving antenna S_r can be derived, again assuming an isotropic emissivity of the target.

$$S_r = \frac{\sigma S_t}{4\pi h^2} \tag{1.2}$$

From antenna theory, it can be deduced that the antenna gain is proportional to the reciprocal of the wavelength λ squared multiplied by the ratio of the power received by the antenna P_r to the incident intensity S_r.

$$g = 4\pi\frac{P_r}{\lambda^2 S_r} \tag{1.3}$$

From the preceding equations, the radar equation for a single backscatterer can be derived, which determines the power received by the antenna P_r as a function of the transmitted power P_t, the height h, and the characteristics of the reflecting target σ.

$$P_r = \frac{g^2 \lambda^2}{(4\pi)^3} \frac{\sigma P_t}{h^4} \tag{1.4}$$

In a next step, the radar equation is extended for a volume with many backscattering targets, since the aim is to determine the received power P_r from a large number of hydrometeors. The scattering volume δV at height h above the radar antenna depends on the height resolution δh and the solid angle Ω of the beam aperture.

$$\delta V = h^2 \Omega \delta h \tag{1.5}$$

Assuming that the distances between the scatterers are sufficiently large, the total cross section of a scattering volume can be condensed to the sum over the single target cross sections σ_i. Lets introduce the volume backscatter coefficient η, which is defined as the total cross section of a scattering volume divided by its volume δV.

$$\eta = \frac{\sum_i \sigma_i}{\delta V} \tag{1.6}$$

Finally, considering these relationships, the radar equation can be determined, which gives the received power P_t from a scattering volume containing many backscattering targets.

$$P_r = \frac{g^2 \lambda^2}{(4\pi)^3} \frac{P_t}{h^2} \eta \Omega \delta h \tag{1.7}$$

Further reading on radar theory and a complete derivation of the radar equation can be found in the following books [5], [31].

1.2 Radar Reflectivity Factor

To define the radar reflectivity factor Z, the cross section according to Rayleigh theory is assumed.

$$\sigma_{\text{Rayleigh}} = \frac{2\pi^5}{3\lambda^4} |K|^2 D^6 \tag{1.8}$$

The material specific parameter $|K|$ is a complex quantity defined in terms of the refractive index n. Based on the Rayleigh cross section σ_{Rayleigh} and the definition of the volume backscatter coefficient (Eq. 1.6), one can deduce the volume

backscatter coefficient η_{Rayleigh} for Rayleigh scattering.

$$\eta_{\text{Rayleigh}} = \frac{2\pi^5}{3\lambda^4}|K|^2 \underbrace{\frac{\sum_i D_i^6}{\delta V}}_{Z} \tag{1.9}$$

From this, the radar reflectivity factor Z is defined as the sum over the sixth power of the diameters of all droplets divided by the backscatter volume, which in the continuous form is equivalent to an integration of the sixth power of the diameters multiplied by the droplet size distribution.

$$Z = \int_0^\infty N(D)D^6 dD \tag{1.10}$$

CHAPTER 2

Micro Rain Radar

The MRR is a frequency modulated continuous wave (FMCW) radar manufactured by Meteorologische Messtechnik (METEK) GmbH. A summary on the technical features for the MRR 2 used in this work can be found in Tab. 1.
The MRR operates with electromagnetic radiation at a central frequency of 24.23 GHz and thus belongs to the K-band radars. The modulation range extends from 0.5 to 15 MHz, which corresponds to a height resolution of 300 m - 10 m.
The radar emits radiation vertically into the atmosphere, of which a part is scattered back to the antenna by any kind of hydrometeors. Due to the fall velocity of the hydrometeors relative to the antenna, a frequency shift between the emitted and the received backscattered signal can be measured (Doppler frequency). This frequency shift is linked to the fall velocity of the hydrometeors, of which their diameter can be inferred. If the intensity of the backscattered signal and the diameters of the hydrometeors are known, their quantity can be calculated.
However, because precipitation consists of hydrometeors with different diameters and thus different terminal velocities, the backscattered signal is a distribution made of varying Doppler frequencies. The remedy is the spectral analysis of the backscattered signal which gives a power spectrum distributed over a range of frequency lines corresponding to the Doppler frequencies.
The following section describes the operating principle of the MRR in more detail.

Operating mode	FMCW Doppler
Center frequency (f_0)	24.23 GHz
Frequency modulation (B)	0.5 - 15 MHz
Number of range gates (N)	32
Number of spectral bins (M)	64
Sampling Frequency f_s	125 kHz
Sweep duration T	256 μs

Table 1. Main technical features of the MRR 2. For further specifications see [19]

2.1 Operating principle for a point target

The Micro Rain Radar is a frequency modulated continuous wave radar. To achieve range resolution, the emitted signal is frequency modulated and the range of the target (or the time delay of the received echo) is derived from the frequency shift between the echo and the emitted signal. The frequency is sawtooth modulated so the frequency sweeps linearly from $f_0 + B/2$ to $f_0 - B/2$ and jumps back to the initial value. Let us first look at the operating principle for a resting point target. For a resting point target, the incoming echo follows with a time delay of t_h.

$$t_h = 2\frac{h}{c} \tag{2.1}$$

In the case of the MRR, $t_h \ll T$ holds, thus the frequency shift can be related to the delay time via the following relationship (illustrated in Fig. 1).

$$\Delta f = \frac{B}{T} t_h \tag{2.2}$$

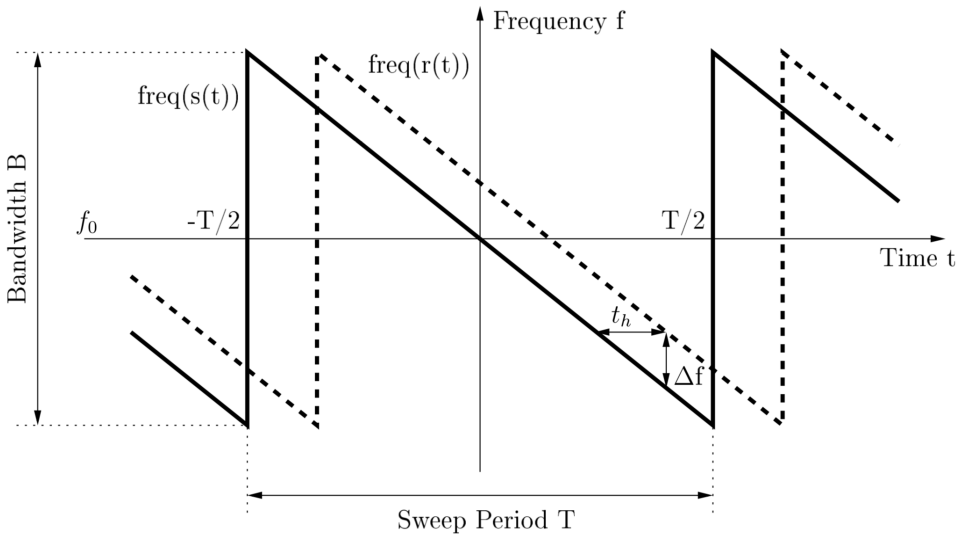

Figure 1. Relation between delay time t_h and frequency shift Δf for a FMCW radar. (Figure taken from [16])

Combining Eq. 2.1 and Eq. 2.2 results in a correlation that allows us to determine the height of a resting point target.

$$h = \frac{cT}{2B} \Delta f \tag{2.3}$$

As the signal of one sweep is a rectangular function of width T, the signal is convoluted with a sinc function in the frequency domain with the first zero appearing at $\pm\frac{1}{T}$, this means that we will only be able to separate frequency components that are at least spaced by the inverse of the width.

$$\delta f = \frac{1}{T} \tag{2.4}$$

Substituting the frequency resolution into the differential form of Eq. 2.3, one can obtain the height resolution.

$$\delta h = \frac{1}{2}\frac{c}{B} \tag{2.5}$$

The MRR operates with a modulation range of 0.5 - 15 MHz, thus the height resolution can be set in the range of 300 m - 10 m.

The maximum resolvable frequency shift by the radar module depends on the sampling frequency f_s, according to the Nyquist criterion the maximum resolvable frequency shift is $f_s/2$. By evaluating the maximum resolvable frequency shift in Eq. 2.3, the maximum detectable height is obtained.

$$h_{\max} = \frac{cT}{2B}\frac{f_s}{2} \tag{2.6}$$

In the further considerations we look at the signal of a moving point target. For a moving point target, the frequency shift of the incoming echo contains an additional Doppler component.

$$\Delta f = \underbrace{B\frac{2h}{cT}}_{\text{height}} \pm \underbrace{\frac{2}{\lambda_0}v}_{\text{Doppler}} \tag{2.7}$$

Note that from the analysis of a single sweep, the velocity cannot be extracted because it overlaps with the height component, but the use of multiple sweeps provides a solution to this problem. The procedure for extracting the velocities is as follows, the signal of a sweep is Fourier transformed, the result is a line spectrum with N lines that represent the signals from N height gates. Each height gate is centered on the frequency $f_N = N/T$ corresponding to a specific height.

$$h_N = N * \delta h \tag{2.8}$$

In a next step, consider a series of M sweeps, each with N lines, from which a $M \times N$-matrix can be constructed. A second Fourier transformation is performed

along each height range gate which yields the Doppler component of the frequency shift f_D and thus the corresponding velocity distribution of the particles at the corresponding height.

The resolution of the Doppler component f_D is equal to the inverse of the acquisition time for a set of spectra τ, where $\tau = 2NM/f_s$.

$$\delta f_D = \frac{1}{\tau} \tag{2.9}$$

Combining this result with the relationship between velocity and Doppler frequency shift Eq. 2.7, the velocity resolution can be determined.

$$\delta v = \frac{\lambda_0}{2}\frac{1}{\tau} \tag{2.10}$$

The maximum resolvable Doppler component depends on the sweep duration, since with each sweep we acquire one sample for each height gate, the Nyquist theorem then states that the maximum is half the inverse of the sweep duration $f_{D_{\max}} = 1/2T$. Placing the maximum resolvable Doppler frequency shift into the relationship between velocity and Doppler frequency shift gives the maximum detectable velocity.

$$v_{\max} = \frac{\lambda_0}{2}\frac{1}{2T} \tag{2.11}$$

After the second Fourier transform, each velocity gate is centered on the Doppler frequency $f_M = M/\tau$, which equals a specified velocity.

$$v_M = M * \delta v \tag{2.12}$$

Overall, we obtain $M \times N$ values for a measured set of spectra, where the spectrum within a height gate consists of a distribution of lines corresponding to the velocity distribution of raindrops.

2.2 Derivation of Drop Size Distributions

The result of the second Fourier transform is the received spectral power $f(n,i)$ as a function of the height bins ($i = 1...N$) and of the Doppler bins ($n = 0...M$-1). The received power is proportional to the reflectivity of all hydrometeors in the backscattering volume within the Doppler frequency resolution, as shown in the radar equation Eq. 1.7.

$$f(n,i) = \frac{10^{20} \cdot \mathrm{TF}(i)}{C}\frac{1}{i^2 \delta h}\eta(n,i) \tag{2.13}$$

TF(i) and C are the transfer function and the calibration constant, they are needed to convert the engineering units of the receiver signal to physical units, both are factory set. In a next step, the received spectral power $f(n,i)$ is converted into the volume backscatter coefficient $\eta(n,i)$ (defined in Eq. 1.6) according to the equation proposed by the manufacturer (Eq. 2.13).

In the further procedure, all integrations are replaced by summations over the Doppler spectral lines n, where the lines considered depend on the height gate. More detailed information about which Doppler spectral lines are considered at which heights can be found in Fig. 4.

$$\int_0^\infty g(f)df \rightarrow \sum_{n_{\min(h)}}^{n_{\max(h)}} g(f_n)\delta f_D \tag{2.14}$$

To transform the dependence from spectral power within line n of width δf_D to velocity v, the following conversion must be performed.

$$g(v) = g(f_n)\delta f_D \frac{\partial f_D}{\partial v}\frac{1}{\delta f_D} = g(f_n)\delta f_D \frac{1}{\delta v} \tag{2.15}$$

Following Eq. 2.15, the volume backscatter coefficient can be introduced in terms of velocity.

$$\eta(v,i) = \eta(n,i)\frac{1}{\delta v} \tag{2.16}$$

Here it is important to state that the following considerations only apply to hydrometeors in liquid form, for which the MRR was actually designed. In the further course of the work, however, an alternative method will be presented that also works with non-liquid hydrometeors.

To calculate the drop size distributions, the relationship between terminal fall velocity v and drop diameter D is used, which was found empirically by Gunn and Kinzer [7] and was put into an analytical form by Atlas et al. [2], see Fig. 2. Additionally a generalized form of the relationship is used that includes a height dependent density correction for the fall velocity $\delta v(h)$.

$$v(D)[\mathrm{m/s}] = (9.65 - 10.3 \cdot e^{-0.6 \cdot D[\mathrm{mm}]})\delta v(h) \quad \text{for } 0.109 \leq D \leq 6\,\mathrm{mm} \tag{2.17}$$

The height dependent density correction for velocity is based on the relationship of Foote and Du Toit [4] who found $v \propto \rho^{0.4}$.This relationship, assuming U.S. standard atmosphere conditions for the height dependence of air density, then leads to the correction term used by the manufacturer.

$$\delta v(h) = 1 + 3.68 \cdot 10^{-5}h + 1.71 \cdot 10^{-9}h^2 \tag{2.18}$$

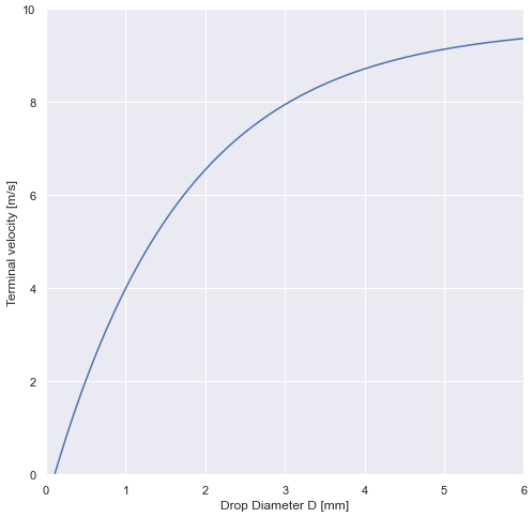

Figure 2. Terminal fall velocity of rain drops at the surface of the earth ($h = 0$) versus the drop size in motionless air (According to Eq. 2.17).

Subsequently, the volume backscatter coefficient is expressed using Eq. 2.17 as a function of drop diameter D instead of velocity v.

$$\eta(D, i) = \eta(v, i)\frac{\partial v}{\partial D} = \eta(v, i) \cdot 6.18 \cdot e^{-0.6 \cdot D}\delta v(i \cdot \delta h) \tag{2.19}$$

Putting everything together and resubstituting v with D we get the complete conversion.

$$\eta(D, i) = \eta(n, i)\frac{1}{\delta v}\frac{6.18}{10.3}(9.65 \cdot \delta v(i \cdot \delta h) - \delta v \cdot n) \tag{2.20}$$

Finally, the drop size distribution $N(D)$, meaning the number of droplets per volume and diameter, can be calculated by dividing the volume backscatter coefficient as a function of droplet diameter $\eta(D, i)$ by the single particle backscatter cross section $\sigma(D)$ of a raindrop with diameter D.

$$N(D, i) = \frac{\eta(D, i)}{\sigma(D)} \tag{2.21}$$

For drop diameters that are small compared to the wavelength, the single particle backscatter cross section can be expressed analytically assuming Rayleigh scattering.

$$\sigma_R(D) = \frac{\pi^5}{\lambda^4}\left|\frac{m^2 - 1}{m^2 + 1}\right|^2 D^6 \tag{2.22}$$

However, not all the drop diameters that occur are small compared to the wavelength of the MRR, so the Rayleigh approximation is not applicable here for all

diameters. Instead, the cross sections are calculated according to the Mie theory, which describes the scattering of an electromagnetic wave from a homogeneous sphere.

Fig. 3 shows the single particle scattering cross sections of water derived from Mie theory relative to those from Rayleigh scattering as used in the MRR drop size retrieval.

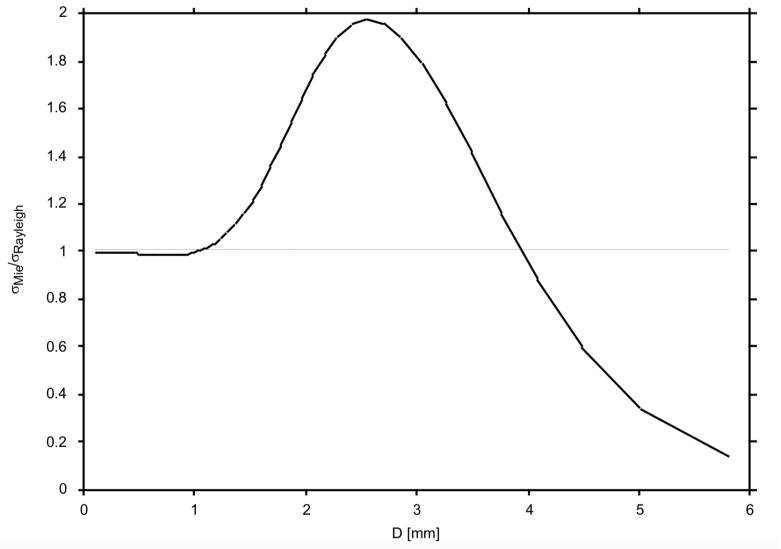

Figure 3. Single particle backscatter cross section of water droplets at 24.23 GHz derived with Mie theory and normalized by Rayleigh backscatter cross section (Figure taken from [20]).

2.3 Derivation of Rain Parameters

Knowing the drop size distribution, we can derive the radar reflectivity factor Z by integrating with the sixth power of the drop diameter, as introduced in section 1.2.

$$Z = \int_0^\infty N(D) D^6 dD \tag{2.23}$$

The reflectivity Z, is the equivalent reflectivity assuming spherical liquid hydrometeors satisfying the Rayleigh approximation. It is a useful quantity in radar meteorology for comparison with other weather radars as it is independent on the wavelength of the systems being operated. In addition, other parameters such as water content or precipitation rate can be derived from the reflectivity factor.

The liquid water content is the product of the total volume of all drops, within the diameter resolution, with the density of water ρ_w divided by the scattering volume. It therefore represents the mass of liquid water per unit volume.

$$LWC = \rho_w \frac{\pi}{6} \int_0^\infty N(D) D^3 dD \tag{2.24}$$

Liquid water content varies greatly from cloud to cloud and can be used to classify clouds.

The rain rate RR is equivalent to the volume of the drop number density $\frac{\pi}{6} N(D) D^3$ multiplied by the terminal fall velocity $v(D)$. From this product, the rain rate is determined by integration over all drop sizes.

$$RR = \frac{\pi}{6} \int_0^\infty N(D) D^3 v(D) dD \tag{2.25}$$

The fall velocity of the drops depends on the drop size. Therefore it is individual for each drop (see Fig. 2). To describe an effective fall velocity of rain, we need to define the characteristic fall velocity. The option chosen by the manufacturer is the first moment of the radar reflectivity factor, which corresponds to the first moment of the Doppler spectrum assuming Rayleigh scattering.

$$W = \frac{\int_0^\infty N(D) D^6 v(D) dD}{\int_0^\infty N(D) D^6 dD} \tag{2.26}$$

2.4 Spectral processing and Noise estimation

A single power spectrum contains a large variance because it consists of a large number of signals from randomly distributed targets in the scattering volume. Therefore, the average is taken over ensembles of power spectra. Averaging over n power spectra reduces the standard deviation by $1/\sqrt{n}$ in the limit of $n \gg 1$.

In addition to the signal from the echo, there is also some noise in the signal, if you were to ignore this, you would see an apparent rain rate. Therefore, noise estimation is performed according to the method of Hildebrand and Sekhon [11]. It is assumed that the noise is white noise, which means that it is independent of the frequency.

The noise estimation algorithm sorts a single Doppler spectrum by amplitude and removes the largest bin until the squared mean of the spectrum E divided by its variance V is greater than or equal to the number of time-averaged spectra n.

$$\frac{E^2}{V} \geq n \tag{2.27}$$

The remaining spectrum is then considered as white noise, and the estimated noise level is equal to its mean, which is then subtracted from the observed Doppler spectrum.

Not all Doppler bins of a Doppler spectrum are used for the determination of the noise and the further calculations. In Fig. 4 the used Doppler bins are displayed depending on the height.

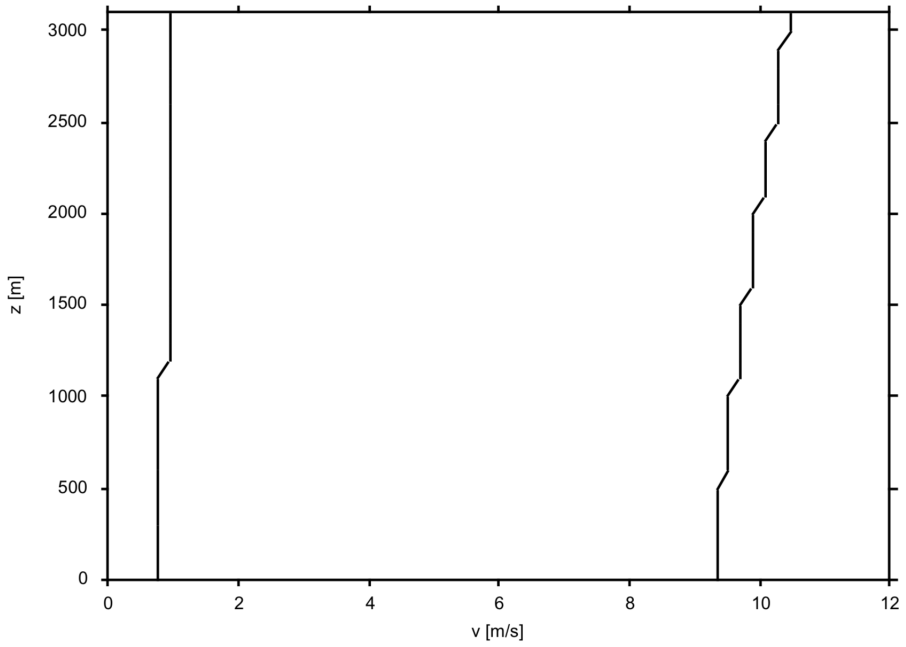

Figure 4. Doppler bins used for the processing as a function of height (Figure taken from [20]).

2.5 Attenuation correction

The intensity of radio waves that propagate through the atmosphere is attenuated by various factors in the atmosphere. The major factor occurs as a consequence of moderate and higher rainfall, which leads to a significant attenuation when high altitudes are taken into account. Therefore, an attenuation correction for rain is carried out according to the method of Peters et al. [28], which was developed for the MRR. All other attenuation factors are neglected.

The attenuation coefficient κ of the power density S is defined as the decrease of the power density by distance.

$$\frac{dS}{dx} = -\kappa(x)S \tag{2.28}$$

Solving the differential equation and taking into account that the damping acts twice because the radar waves travel up and down the range r, the path-integrated attenuation **PIA** can be established.

$$\mathbf{PIA}(r) = e^{2\int_0^r \kappa(x)dx} \tag{2.29}$$

PIA is a common factor for all drop sizes, therefore it can be taken out of all attenuated integral variables ξ_a (Z, LWC, RR and W). Where the subscript a stands for not attenuation corrected.

$$\xi = \xi_a \mathbf{PIA} \tag{2.30}$$

The attenuation coefficient κ_a, but not attenuation corrected itself, is obtained from the integral over all diameters of the product of the single-particle extinction cross section σ_e with the drop size distribution.

$$\kappa_a = \int_0^\infty \sigma_e(D)N(D)dD \tag{2.31}$$

Considering Eq. 2.29 and Eq. 2.30, the path-integrated attenuation can be expressed by the uncorrected attenuation coefficient κ_a. A detailed derivation of Eq. 2.32 can be found in [28].

$$\mathbf{PIA}(r) = \frac{1}{1 - 2\int_0^r \kappa_a(x)dx} \tag{2.32}$$

The previous equation (Eq. 2.32) requires that κ_a can be measured with infinitesimal range resolution, but the MRR measures spatial averages over the range resolution δh. Replacing the integral by the corresponding sum over the range gate depth δh would lead to a biased attenuation correction. But assuming that the scattering volume is homogeneously filled, meaning that $N(D)$ is independent of the range x within the scattering volume, an unbiased attenuation correction can be obtained (shown by Peters et al. [28]). The procedure is given hereafter.

Beginning the calculation in the first range gate $r = 1$, assuming $\mathbf{PIA}(r_0) = 1$, the drop size distribution corrected for the attenuation on the path between the radar and the lower boundary of range gate r_i, but without the correction of attenuation within r_i (subscript p), is derived.

$$N_p(D, r_i) = N_a(D, r_i)\mathbf{PIA}(r_{i-1}) \tag{2.33}$$

Based on this, the partial attenuation corrected attenuation coefficient κ_p is obtained.

$$\kappa_p(r_i) = \sum_{\min(D)}^{\max(D)} \sigma_e(D) N_p(D, r_i) \delta D \tag{2.34}$$

In the succeeding step the drop size distribution corrected for the attenuation within the range gate r_i is calculated. A detailed derivation of Eq. 2.35 can be found in [28].

$$N(D, r_i) = -N_p(D, r_i) \frac{\log(1 - 2\kappa_p(r_i)\delta h)}{2\kappa_p(r_i)\delta h} \tag{2.35}$$

Using the corrected drop size distribution, the corrected damping coefficient κ can be determined.

$$\kappa(r_i) = \sum_{\min(D)}^{\max(D)} \sigma_e(D) N(D, r_i) \delta D \tag{2.36}$$

In a last step, the path-integrated attenuation value is calculated up to the range gate r_i.

$$\mathbf{PIA}(r_i) = \mathbf{PIA}(r_{i-1}) e^{2\kappa(r_i)\delta h} \tag{2.37}$$

This procedure is continued stepwise until the highest range gate is reached.

CHAPTER 3

Micro Rain Radar Data

The MRR was deployed in March 2007 as part of Andreas Leuenberger's master's thesis. It is located on the campus of the University of Bern (N46.95° E7.44°) on the ExWi building at an altitude of 575 m above sea level (a.s.l.). Since then, it has been in continuous operation and collects data, but with some interruptions of varying duration for reasons that are partly explained and partly unexplained.

3.1 Data situation

The MRR's measurement data is stored in different locations and in different formats. This section will give a brief overview of where and in what form the data is available.

The data between the years 2007 and 2015 are available on MySQL in an easily accessible form. It should be noted that between November 2008 and December 2009, the MRR's height resolution was set to 50 m instead of the usual 100 m, which reduces the maximal detected height to 1500 m. Data from 2015 to the present can be found on the institute's data portal [32], but not in an easily accessible form. This means that all measurement data are written daily into a new text file and these text files can be found on the institute's data portal.

3.2 Data structure

Three different data sets are stored by the MRR. One of them is the raw data set containing the spectral powers for each measured altitude with a temporal resolution of 10 seconds. Next is the instantaneous data set, which consists of processed data such as rainfall rates, radar reflectivity and other precipitation parameters. It is similarly recorded with a temporal resolution of 10 seconds. Finally, there is the averaged data set. It also contains processed data, like the instant data set, but it is calculated by raw data which is averaged over one minute.

For the instant data and the averaged data there is a conditional recording, meaning that there is only data stored on the server if the processing software detected precipitation during the measuring interval.

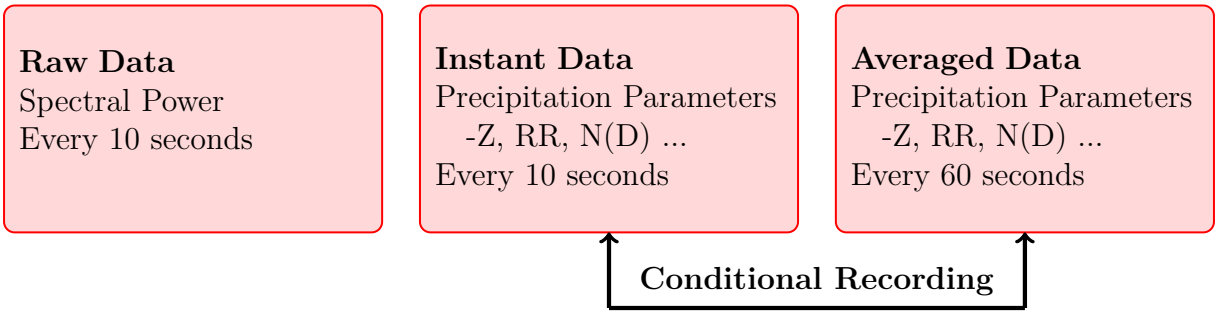

Figure 5. Data structure

CHAPTER 4

Review of the MRR data

In this chapter a review of the processed MRR data is presented, covering the years 2008 to 2013. For this purpose, the precipitation rates (by the manufacturer labelled as rain rates - RR) measured by the MRR at an altitude of 0 - 100 m a.g.l. were compared with the precipitation rates measured by two tipping buckets. Similarly to the radar, one of the tipping buckets is located on the roof of the ExWi building and is maintained by the institute. The other tipping bucket is located at Bern-Bollwerk, which is less than 200 m straight-line distance apart, and is maintained by the Bundesamt für Umwelt (BAFU). The precipitation rates were used for the comparison because they allow both the accuracy and the temporal completeness to be checked.

4.1 Diurnal recorded precipitation

The MRR's raw data should actually be recorded continuously, after which it should be simple to evaluate periods during which the device was operating. However, it turned out that the raw data for the investigated years was also conditional recorded (See section 3.2). Due to the conditional recording, cross comparisons with other data sets were necessary to find gaps in the recordings or in the processing.
The following Figures (6, 7, 8) display the diurnal recorded precipitation measured by the MRR. The hours at which precipitation was recorded are indicated in color. Marked in grey are those hours at which both tipping buckets recorded precipitation, but for which no precipitation can be found between 0 - 100 m in the instant data of the MRR. The hours in which neither the tipping buckets nor the radar detected any precipitation were left white.

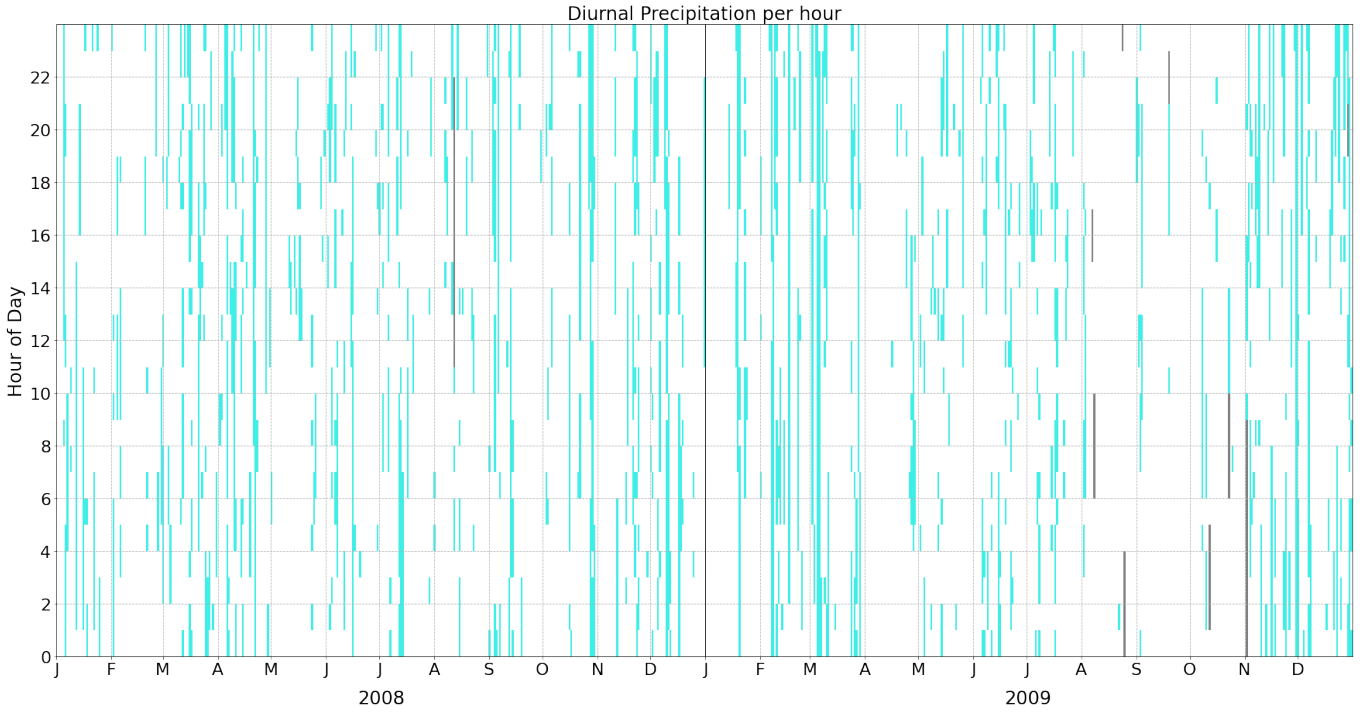

Figure 6. Diurnal recorded precipitation for each hour in 2008 and 2009

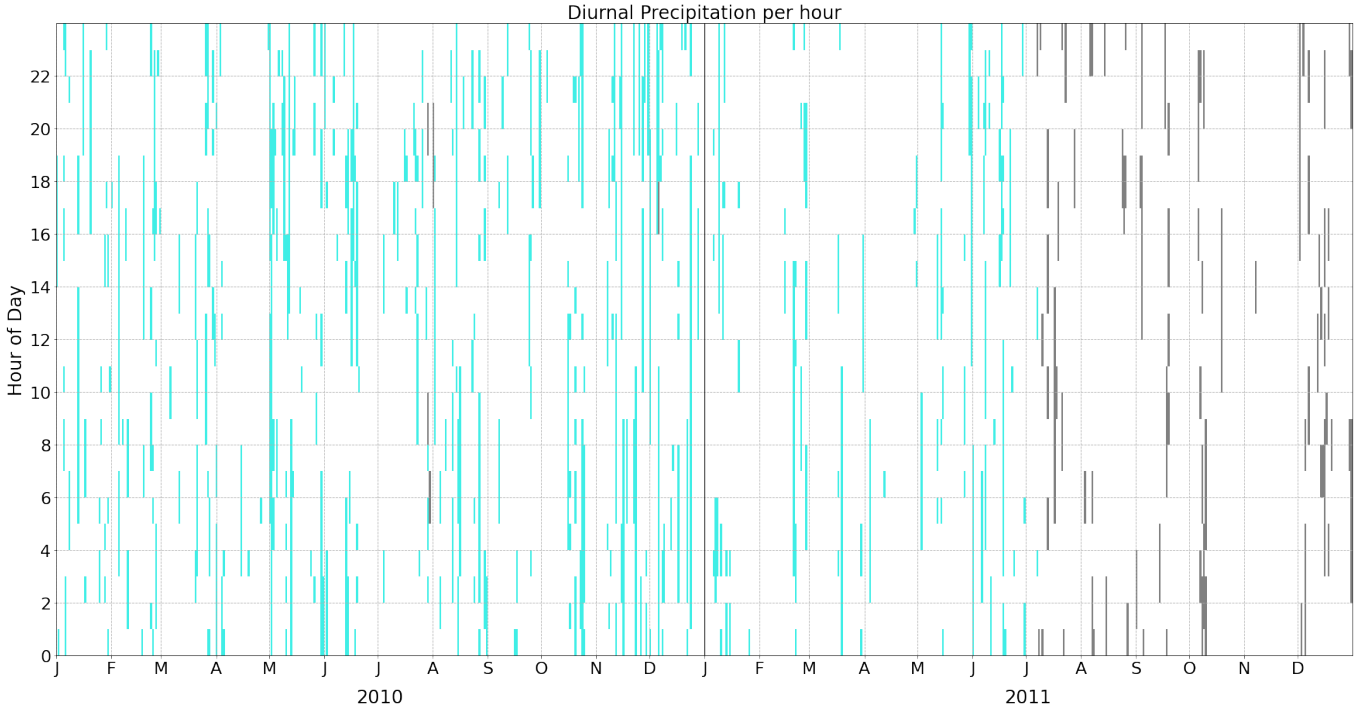

Figure 7. Diurnal precipitation recorded for each hour in 2010 and 2011

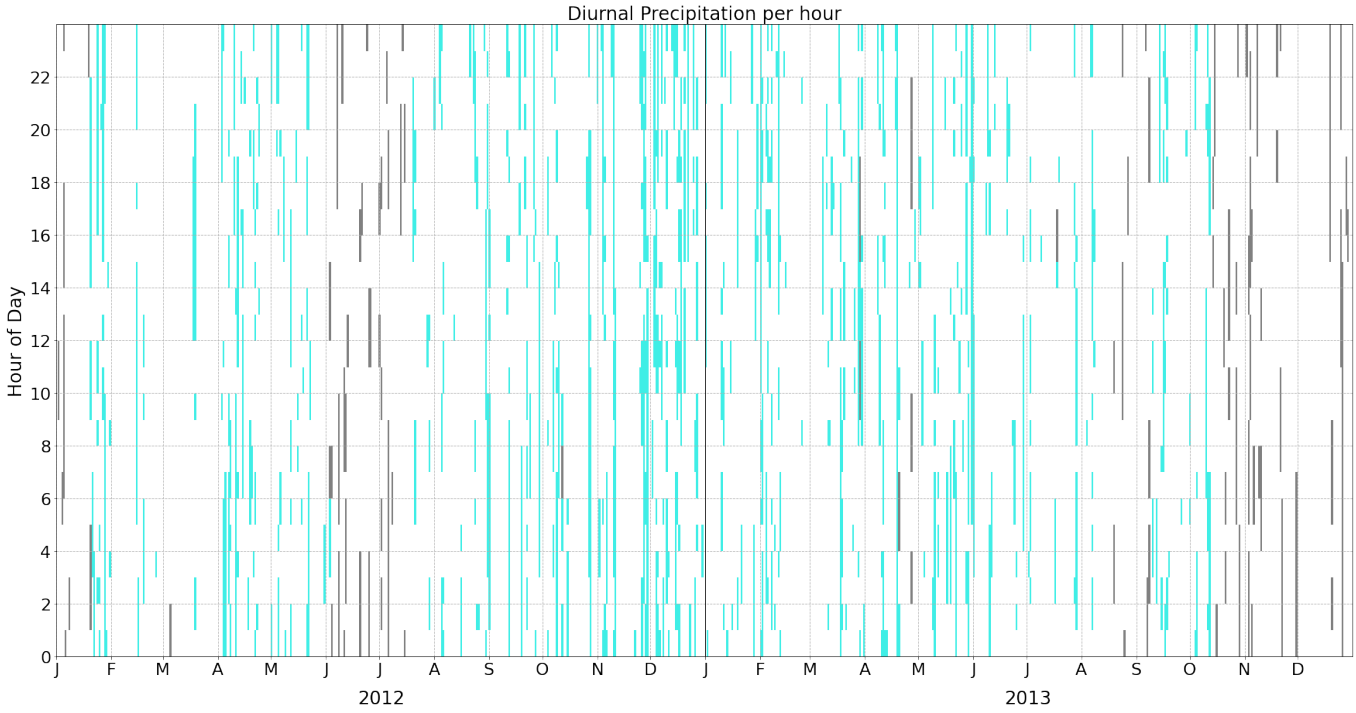

Figure 8. Diurnal precipitation recorded for each hour in 2012 and 2013

It is evident from the figures that the MRR operated very reliably in 2008 and 2009. The number of downtime hours is marginal for the duration of two years. The picture is the same for 2010, with very few downtime hours. In contrast, there is a large gap in 2011, marked by the numerous grey entries, starting at the beginning of July and ending in January 2012. In addition, there exists a gap for the months of June and July in 2012. In 2013, the radar operated more reliably again, at least until mid-October.
In case of missing or corrupted instant data, it could be because the MRR did not operate at all, due to network errors or times when the MRR computer was stuck and a restart was forgotten, in this case both the instant and the raw data would be completely missing, but it could also be because the raw data was processed improperly, which means that there could be error-free raw data. It should be noted here that from this comparison, it can only be concluded that the instant data is missing or corrupted, but no conclusion can be inferred about the condition or existence of the raw data.

4.2 Monthly recorded precipitation

To evaluate the accuracy of the instant data, we compared the monthly total precipitation measurements. For this purpose, the precipitation amounts measured by the tipping buckets and the MRR in the lowest height gate were converted into monthly precipitation amounts.
Figures 9 and 10 present the monthly recorded amounts of precipitation by the individual instruments over the period from 2008 to 2013. In addition, the precipitation amounts measured by the tipping bucket on the ExWi building (marked in grey and labelled "added") were added to the precipitation amounts measured by the radar at the times when the radar was not in operation (determined in the previous section). This was made in order to gain an impression of the quality of the precipitation measurements even during the months in which the MRR was only partially operable.

Figure 9. Monthly recorded precipitation in 2008, 2009 and 2010

Figure 10. Monthly recorded precipitation in 2011, 2012 and 2013

In the data for the first half of 2008, a large gap for the tipping bucket on the ExWi building is evident, therefore the data from the tipping bucket at Bern-Bollwerk were added to the analysis.
The measured monthly precipitation amounts by the different devices often show an acceptable agreement. However, it is striking that the MRR totally overestimates the precipitation amounts between the months of November and March. We suspect that this is due to the fact that during these months precipitation falls more frequently in the form of snow or sleet.
In case of snow or sleet, the MRR may totally overestimate the precipitation rates. This is because its data processing is designed for liquid precipitation. The overestimation of precipitation rates may be due to the following reasons. In sleet or wet snow the hydrometeors have a much greater reflectivity than in liquid rain for the same reason as in the case of the bright band (see Appendix), this leads to an overestimation of the number N of hydrometeors. The fall velocity of snow is much more sensitive to turbulences, therefore frozen hydrometeors can also have upward velocities. These upward velocities are misinterpreted by the MRR as very

fast downward velocities (more detailed in section 5.1.2). Looking at Eq. 2.25, we see that both lead to an increased measured precipitation rate.
Improved methods for calculating snow rates from MRR data are discussed by Kneifel et al. [14] and by Maahn and Kollias [17].
In July 2009 there is also a clear difference in the monthly precipitation amounts between MRR and tipping buckets. We cannot give an exact explanation for the cause, but we suspect that it is related to heavy storms. On 4 July 2009, thundershowers were reported, which led to property damage, and on 23 July 2009 hail was reported with grain sizes of 2 - 4 cm (reported in [1] and [12]).
We do not know exactly how hail is detected by the MRR, nor are we aware of any studies from the literature. But we also do not know how accurate tipping buckets are able to measure hail.

4.3 Conclusion on the data

In conclusion the MRR operated reliably in the years from 2008 to 2010. The measured rainfall amounts, if liquid, and the number of precipitation hours for these years are mostly consistent with the measurements of the two rain gauges, as can be seen from the Figures 6, 7, 9.
In the following years from 2011 to 2013, there are increasingly large gaps in the processed data, see Figures 7, 8. However, we suspect that at these times the raw data is not corrupted but that there was an error in the data processing, but this has not been conclusively determined. From 2014 to the present, the MRR has been operating more and more unreliably. The query of the data revealed that although raw data is available, the processed data is almost always completely missing. The reason why the processing of the raw data by the MRR itself does not work has not been clarified but we suspect that it is due to a shortcoming in the METEK software.

As of the end of 2009, occasionally the MRR's data processing did not work properly. In the Figures 11 and 12 there are two examples where entries are missing in the processed data (the white fields are the missing entries). In the figures the radar reflectivity is shown, but any precipitation parameters are missing when the data processing did not work properly.
There are repeated periods in the data where the processed data are missing from a certain altitude on, and it is not always from the same altitude, as can be seen in the figures. We do not know exactly where the error lies for the missing data, whether it is in the data transmission or in the processing of the raw data. However, there are no errors in the raw data at these times. It was therefore decided to install a new data processing.

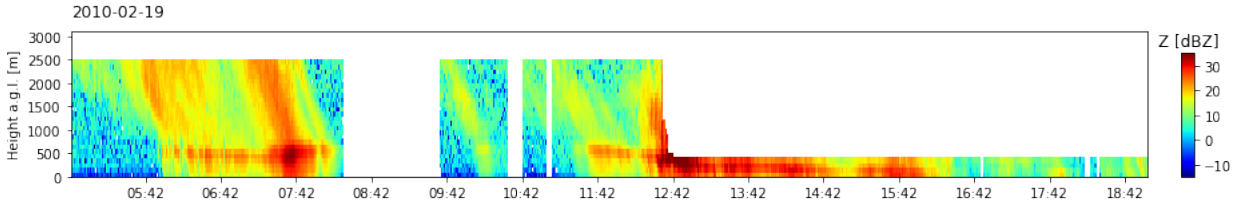

Figure 11. Disturbed processed data from February 19, 2010. The data is completely missing above a certain altitude.

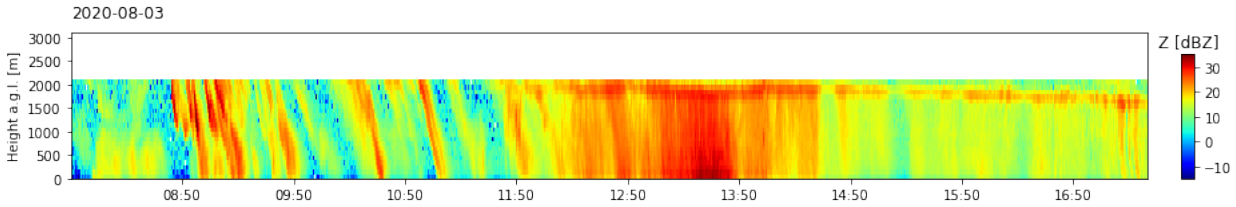

Figure 12. Disturbed processed data from August 3, 2020. The data is completely missing above a certain altitude.

CHAPTER 5

Data Processing

The processing of the raw data, which was presented in chapter 2, is carried out by the Micro Rain Radar itself. However, not only processed data is recorded but also the raw data. This creates the possibility for researchers to create their own data processing. In this way, the potential of the MRR can be better exploited. The data processing can be adapted to the latest state of research and supplemented for the derivation of other variables. The radar can thus also be used for purposes other than precipitation monitoring (Voge and Hort use the MRR to monitor a volcano [34]).

Such alternative raw data processing has been developed, for example, by Maahn and Kollias [17], which is particularly suitable for monitoring snow precipitation. Their developed processing methodology improves sensitivity through enhanced noise reduction. Using a newly introduced Doppler dealiasing, it can detect upward movements of precipitation, which means precipitation moving away from the radar.

Another alternative raw data processing is made available by Garcia-Benadi et al. [6]. The methodology defines the derived variables more precisely by prior classification of precipitation type into snow, drizzle, rain, hail and mixed precipitation. It also includes improved noise level determination, peak signal detection and Doppler dealiasing, which allows the upward motion of precipitation particles to be taken into account.

For the new data processing we decided to use the methodology of Garcia-Benadi et al. because of its wide range of applications, such as the extension of precipitation measurement for snow and its significant advantages over MRR's own data processing provided by METEK.

In the further course of this chapter we will introduce the Improved Doppler Spectral Processing Methodology by Garcia-Benadi et al.

5.1 Improved Doppler Spectral Processing Methodology

Like the MRR's own processing, the methodology starts by calculating the volume backscatter coefficient $\eta(n, i)$ from the spectral power $f(n, i)$ according to Eq. 2.13. On these, a peak signal detection and a noise level determination are performed.

5.1.1 Peak Signal Detection and Noise Level Determination

The noise and the peak value for the volume backscatter coefficient $\eta(n, i)$ are determined individually for each height. For this purpose, all Doppler bins of the spectrum except the first and the last one are used, so compared to MRR's own noise determination, fewer Doppler bins are ignored (compare with Fig. 4). Hence, all possible fall velocity values are used, except the lowest and the highest. This approach makes it easier to detect multi-peaks in the signal. In a next step, the peaks are determined, they are defined by the condition that the values in the preceding and the following bin exist and are less than the peak value itself. Afterwards, all values greater than the maximum peak value are removed. This is done primarily to eliminate large noise peaks near the ground. It is after these steps that the methodology applies the actual noise determination and removal, according to the method of Hildebrand and Sekhon [11], this is the same method used by MRR's own processing methodology. Finally, after noise removal, any value that does not belong to a series of at least three consecutive existing entries is removed.

In a next step, the volume backscatter coefficient is expressed as a function of velocity instead of Doppler bins according to Eq. 2.16. Afterwards, a Doppler dealiasing is applied to them.

5.1.2 Doppler Dealiasing

The velocity resolution of MRR's own processing methodology is limited to a range of 0 - 12.3 m/s. With the help of the dealising scheme used, this range can be extended in Garcia-Benadi's processing methodology to a range from -12.3 to 24.6 m/s. The scheme used combines, for a given height, information from spectra of neighbouring height levels (upper and lower) to obtain the fall velocities of the hydrometeors.

In a first step, the noise corrected Doppler spectrum (Fig. 13 (**a**)) is enlarged to the velocity range −12.3 - 24.6 m/s by duplicating the original spectrum into the upper and lower velocity range gates (Fig. 13 (**b**)). As a result, there are up to three different possible spectra. To find the correct spectrum, a provisional radar equivalent reflectivity Z_e is determined (using the non dealiased spectrum) from which an expected mean velocity can be deduced using Eq. 5.1 and Eq. 5.2 from Atlas et al. [2].

$$v_{Rain} = 2.65 \cdot Z_e^{0.114} \tag{5.1}$$

$$v_{Snow} = 0.817 \cdot Z_e^{0.063} \tag{5.2}$$

Subsequently, the velocities of the vertically continuous spectra are compared with the fall velocities calculated from the spectral reflectivity. The spectrum with the smallest difference is read out as the most probable one (Fig. 13 (**c**)).

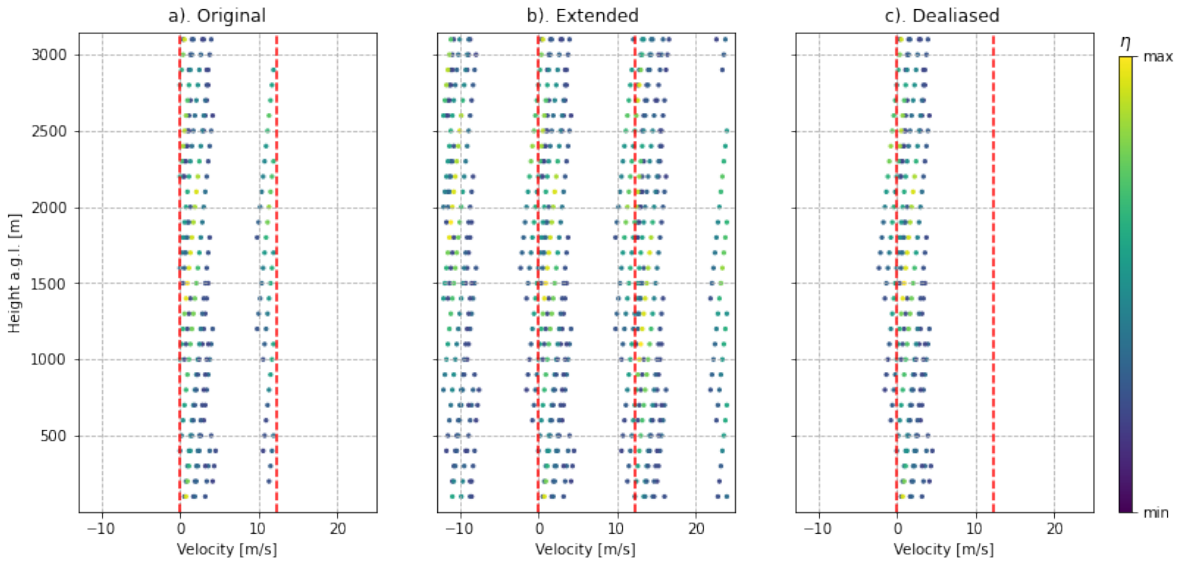

Figure 13. Schematic of Doppler dealiasing, shown is the volume backscatter coefficient η after noise extraction. Measurement from June 23, 2010

Doppler dealiasing can largely improve precipitation measurements. Because due to the aliasing effect, small upward velocities of hydrometeors are misinterpreted by the MRR as very fast downward movements. Also through the aliasing effect, fall velocities that are larger than the maximally detectable velocity are seen as small downward velocities. Both lead to incorrect precipitation rates.

5.1.3 Parameters Calculation

Once the spectra have been dealiased, the following parameters are calculated, which depend only on the volume backscatter coefficient η and which are independent of the type of precipitation. These are the radar equivalent reflectivity Z_e, the effective fall velocity W, and higher order moments of the velocity distributions (variance σ, skewness sk and kurtosis) which are relevant for the determination of the precipitation type.

$$Z_e = 10^{18} \cdot \frac{\lambda^4}{\pi^5} \cdot \frac{1}{|K^2|} \int_{-\infty}^{\infty} \eta(v) dv \tag{5.3}$$

$$W = \frac{\int_{-\infty}^{\infty} v \cdot \eta(v) dv}{\int_{-\infty}^{\infty} \eta(v) dv} \tag{5.4}$$

$$\sigma = \sqrt{\frac{\int_{-\infty}^{\infty} \eta(v) \cdot (v - w)^2 dv}{\int_{-\infty}^{\infty} \eta(v) dv}} \tag{5.5}$$

5.1.4 Bright Band Detection

The next step is to check whether there is a bright band and if so, at what height it is located. Because the presence or absence of a bright band, as well as its height and thickness, are important parameters for classifying precipitation types and distinguishing between convective and stratiform precipitation. The bright band detection algorithm first checks whether a bright band is present or not, following the method of Cha et al. [3]. For this purpose, the height of the peak reflectivity H_{peak} is introduced, which is defined as the height at which the gradient of Z_e is positive for the last time before turning negative. Furthermore, the preliminary bright band upper height H_T and lower height H_B are determined as the height at which the gradient of Z_e assumes the largest negative respectively the largest positive value. Then a bright band is present if H_{peak} is defined and if it is both higher than the preliminary lower height H_B and lower than the preliminary upper height H_T.

$$H_B < H_{\text{peak}} < H_T \tag{5.6}$$

Given that this condition is fulfilled, the algorithm determines the bottom and top height of the bright band according to the method of Wang et al. [35]. According to which the bright band bottom is located where the gradient of the effective fall velocity reaches its maximum value. The bright band top, on the other hand, is

defined as the height of the maximum value of the gradient of reflectivity above the bright band bottom.

5.1.5 Precipitation Type Classification

Finally, a precipitation type classification is carried out for each height bin. The processing methodology distinguishes between five possible precipitation types for each height bin, namely drizzle, rain, snow, mixed and hail. Whereby in the category mixed, wet snow, a mixture of snow and rain and sleet are grouped together.
The classification is built on a decision tree that considers relationships between the fall velocity of the hydrometeors, the equivalent radar reflectivity, the higher order moments of the velocity distributions and the existence or absence of the bright band. A detailed description of the decision tree can be found in [6].
Once the precipitation type has been determined, an attenuation correction is carried out, analogous to MRR's own processing methodology, see section 2.5. Subsequently, further precipitation parameters are determined, depending on the type of precipitation. In case of rain and drizzle, the procedure is analogous to MRR's own processing methodology. In the case of snow or mixed, the snowfall rate SR is calculated using a so-called Z_e-R relation, see Eq. 5.7.

$$SR = \left(\frac{Z_e}{56}\right)^{\frac{1}{1.2}} \tag{5.7}$$

The relation was found empirically by Matrosov and published in 2007 [18]. Further precipitation parameters, namely the liquid water content LWC and the drop size distribution N, are not determined in this case.

5.2 Implementation

As shown, the processing methodology developed by Garcia-Benadi et al. has far-reaching advantages over the standard processing methodology.
In the new data processing that we have implemented, the raw data which are recorded daily by the MRR are first corrected. Because the recorded raw data have errors almost daily, these include missing lines as well as erroneous lines. Finally, the data is processed and stored on the servers. A complete reprocessing of old raw data was not carried out, but old raw data was reprocessed selectively and for the purpose of this work. All MRR data presented in the following chapters were reprocessed using the Garcia-Benadi et al. processing methodology.

CHAPTER 6

Further data used

For the analysis of the virga events, we also used other data besides the MRR data. To get a broader picture of the atmospheric conditions, we added atmospheric reanalysis data from ERA5, as well as atmospheric back trajectories generated by HYSPLIT. In addition, we used data from ceilometers, a device for determining cloud heights. Just like the MRR, the ceilometers are also located on the campus of the University of Bern on the ExWi building.

6.1 ERA5

ERA5 is a global atmospheric reanalysis developed by the Copernicus Climate Change Service (C3S) and produced at the European Centre for Medium-Range Weather Forecasts (ECMWF). An atmospheric reanalysis is a method of creating meteorological data sets using models of weather forecasting and assimilation of observational data (for detailed information on the assimilated observational data see [10]). The weather forecast model used for ERA5 is the Integrated Forecasting System (IFS) Cy41r2 developed by ECMWF.
Various data sets with different variables are then made available from the ERA5 reanalysis, the ones used for this work are the data sets "ERA5 hourly data on pressure levels from 1979 to present" [8] and "ERA5 hourly data on single levels from 1979 to present" [9]. They contain a variety of atmospheric variables, the ones included in this work being temperature, relative humidity, specific humidity, specific rain water content, specific snow water content, total precipitation and horizontal as well as vertical wind speeds. The data sets have a temporal resolution of one hour and a horizontal resolution of 0.25° x 0.25°. The vertical coverage of the first data set ranges from 1000 hPa to 1 hPa, on 37 pressure levels, however in this work the data is expressed in meters above sea level or meters above ground level.
For the conversion to meters above sea level, the geopotential Φ was used, which is the gravitational potential energy of a unit mass at a given location, relative to mean sea level, as given in the ERA5 data for each grid point. As Eq. 6.1 illustrates, with the geopotential and the use of the earth's radius Re, the height

above sea level z can be determined.

$$z = \frac{\mathrm{Re}\Phi}{g\mathrm{Re} - \Phi} \tag{6.1}$$

Subsequently, the data had to be transferred to a new grid, for which the variables were interpolated along the vertical dimension.

6.2 HYSPLIT

The Hybrid Single-Particle Lagrangian Integrated Trajectory Model (HYSPLIT) is a model published by the NOAA Air Resources Laboratory for calculating trajectories of air parcels to determine worldwide the distance and direction in which an air parcel moves. A detailed description of the algorithm can be found in Rolph et al. [29] and a summary of the opportunities that HYSPLIT offers can be found in Stein et al. [30].
The HYSPLIT model can be used among other things to calculate forward and backward trajectories of air parcels. In a forward trajectory, a parcel of air is selected which is located at a certain place on the earth at a certain time, after which the model can predict the vertical and horizontal movement of the parcel of air for a certain period of time. In a back trajectory, an air parcel is selected and the model calculates where the air parcel originates from, in other words, it determines the path of the air parcel backwards in time from the selected location for the selected time.
In addition to the path, the HYSPLIT model can also determine the time evolution of some meteorological variables of the air parcel, such as the relative humidity, the potential temperature or the precipitation of the air parcel. The meteorological data on the basis of which the trajectories are calculated have a coarse temporal resolution of 3 hours, which is why rapidly changing conditions cannot be included in the calculations, furthermore the horizontal resolution of 1° is also quite coarse. All back trajectories presented in this work were generated with the online READY web version of HYSPLIT application, which can be found here [15].

6.3 Ceilometer

A ceilometer is a device with which the height of a cloud base and the vertical visibility can be determined. The ceilometer sends short laser pulses in a vertical direction and measures the backscatter caused by haze, fog, precipitation and clouds. Since the speed of light is known, the backscattered signals can be assigned to a height with the help of the time between sending and receiving a signal (Eq.

6.2).

$$h = \frac{ct}{2} \tag{6.2}$$

The ceilometer then creates a backscatter profile, that is the signal strength in relation to the height measured over a certain period of time. An exemplary backscatter profile is shown in Fig. 14. The laser power used in ceilometers is so low that the noise of the ambient light exceeds the backscattered signal. Therefore, the backscattered signals of several laser pulses are summed, and the noise, which is mostly white noise, partially cancels itself out.

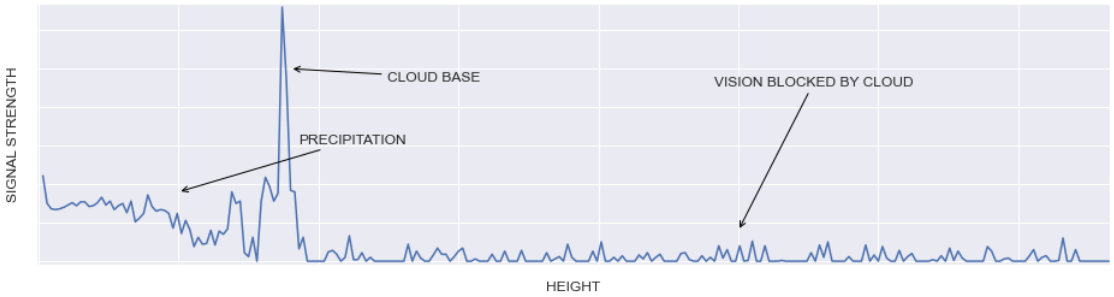

Figure 14. Exemplary backscatter Profile of a Ceilometer. Behind the cloud base, visibility for the ceilometer is severely impaired or blocked by the absorption of the cloud.

The ceilometer data being used in this study originates from two different devices. Data acquired earlier than the year 2015 were obtained from a CT25K by Vaisala, more recent data originate from a CHM 15k by Lufft. The cloud layer height data used in this paper is from an automatic algorithm of the CT25k. Detailed information on the algorithm's functionality can be found in [33].

CHAPTER 7

Virga precipitation

What is virga precipitation? Virga precipitation is precipitation which evaporates or sublimates before it reaches the ground. This phenomenon is sometimes visible by eye as an observable shaft of precipitation that descends from the under surface of a cloud, if that is the case it is called a virga cloud. Virga precipitation can occur in the form of rain, drizzle, snow or ice, depending on the meteorological conditions. It is assumed that this phenomenon occurs mainly when the falling precipitation from a cloud passes through a layer of low humidity causing rapid evaporation or sublimation. For this reason, virga occur often in deserts and semi-arid continental regions shown by Wang et al. [36].

On the topic of virga there exist comparatively few publications, and little can be found in the literature. However, it is important to know what percentage of precipitation reaches the ground. Studies have shown that the number of virga precipitation events in deserts and semi-arid continental regions accounts for over 30% of all precipitation events (Wang et al. [36]). And due to global warming, virga could also occur more often in continental Europe in the near future. The investigation of virga can also be useful for weather forecasting and climate prediction. Important features of virga like the vertical profiles of precipitation rates and evaporation rates, are challenging to parametrize for weather and climate models.

Another phenomenon associated with virga clouds is the dry downburst. A dry downburst is a strong downdraft creating a small-scale divergent wind field at the surface. Such a downburst can cause, for example, the crash of a low-flying aircraft or damage to buildings. It can occur when precipitation falls from a cloud but evaporates or sublimates before it reaches the ground. Because enthalpy of fusion is required to melt, sublimate or evaporate the precipitation, the air cools down. Then the cooler heavy air plunges downward through the warmer lighter air below. This can create strong downdrafts, which are called micro bursts. More detailed information on downbursts can be found in Wilson and Wakimoto [37].

7.1 Search for virga precipitation

To start, we had to look for virga events in the data to determine if any were captured at all. For this purpose, we decided to investigate the MRR data at Bern between 2008 and 2013, because in those data, compared to those of the following years, the data processing worked more reliably.
As virga precipitation occurs in different forms, it is not simple to establish criteria for their search, and due to the few publications on virga events, there are also no uniform standards for doing so. The way we did it was, that we used all the available instant data (processed by MRR's own processing methodology) of those years and searched for events where the MRR measured precipitation rates but not in the lowest three height gates for at least 5 minutes, which means no measured precipitation rates between 0 - 300 m.
As one can imagine, this is not a very limiting criterion. It is also fulfilled by other processes like for example beginning or ending precipitation. This meant that all the events which met our criterion had to be plotted first and then categorized by eye to find suitable examples of virga precipitation. In this way, several virga or virga-like events were found in the MRR data between 2008 and 2013, of which two selected events are presented in more detail in this work.
It was decided not to make a climatology of the occurrence of virga precipitation over Bern, because the data are fragmentary and virga precipitation does not occur sufficiently often that a justifiable statement about its frequency could be derived from the existing data.

7.2 Selection criteria

We have chosen the following events because they last a long time, that means they both extend over several hours, which allows us to combine them with the atmospheric reanalysis data from ERA5, which has a temporal resolution of one hour. It also allows us to rule out the possibility that a possible virga event is only precipitation that grazes the radar's field of view and reaches the ground outside it.
Furthermore, emphasis was placed on having a temporal constant precipitation measurement during the events and to avoid breakthroughs in which precipitation reaches the ground. Because then the virga precipitation was not only local, but horizontally extended and constant, which makes it more likely to link it with the atmospheric reanalysis data, which has a quite coarse horizontal resolution of 0.25°. Lastly, we attached importance to the selection that the measured virga

precipitation would not get near the ground and that the signal would not appear very weak, the former because we wanted to be sure that really no precipitation would reach the ground and the latter because we have no knowledge about the uncertainty of the MRR measurements and we wanted to exclude the possibility that the events are only noise.

7.3 Cloud visibility

One might wonder whether the signals we observe do not actually originate from clouds and consequently represent no virga precipitation after all. But clouds cannot be seen by the MRR, because the MRR is not designed for this purpose. Therefore the signals coming from clouds are not included in the determination of the precipitation parameters. Depending on the processing software, different Doppler bins are used in the raw radar data evaluation, but none uses the first bin $n = 0$ and the last bin $n = 63$ for the calculation of the precipitation parameters (the bins discarded by METEK can be found in Fig. 4 and the processing methodology by Garcia-Benadi et al. discards the bins $n = 1$ and $n = 63$). By discarding the signals of at least the first and the last bin, the signals of targets with velocities in the range of $0 - \delta v$ and the signals with negative velocities in this range, contributing to the last bin by aliasing, are ignored. Thus, only precipitation particles moving towards or away from the radar with at least the velocity δv will be included in the calculations. For liquid precipitation particles, the Gunn and Kinzer relation (Eq. 2.17) then yields a minimum detectable droplet diameter that is larger than the maximal cloud droplet diameter of 0.1 mm (for the methodology of Garcia-Benadi et al. the minimum detectable diameter is $D_{\min} = 0.141\,\mathrm{mm}$ and for METEK $D_{\min} = 0.246\,\mathrm{mm}$). Figures 15 and 16 are two examples of the MRR being unable to detect clouds. They present measurements taken on the 25th of August 2021 and the 28th of August 2021. Displayed are the measured reflectivity of the MRR processed with the method of Garcia-Benadi et al., the distance corrected signal (RCS) of the ceilometer (model CHM 15k) located on the roof of the ExWi building, and an image of a webcam, also mounted on the building, taken at 10:00 UTC (12:00 CEST).

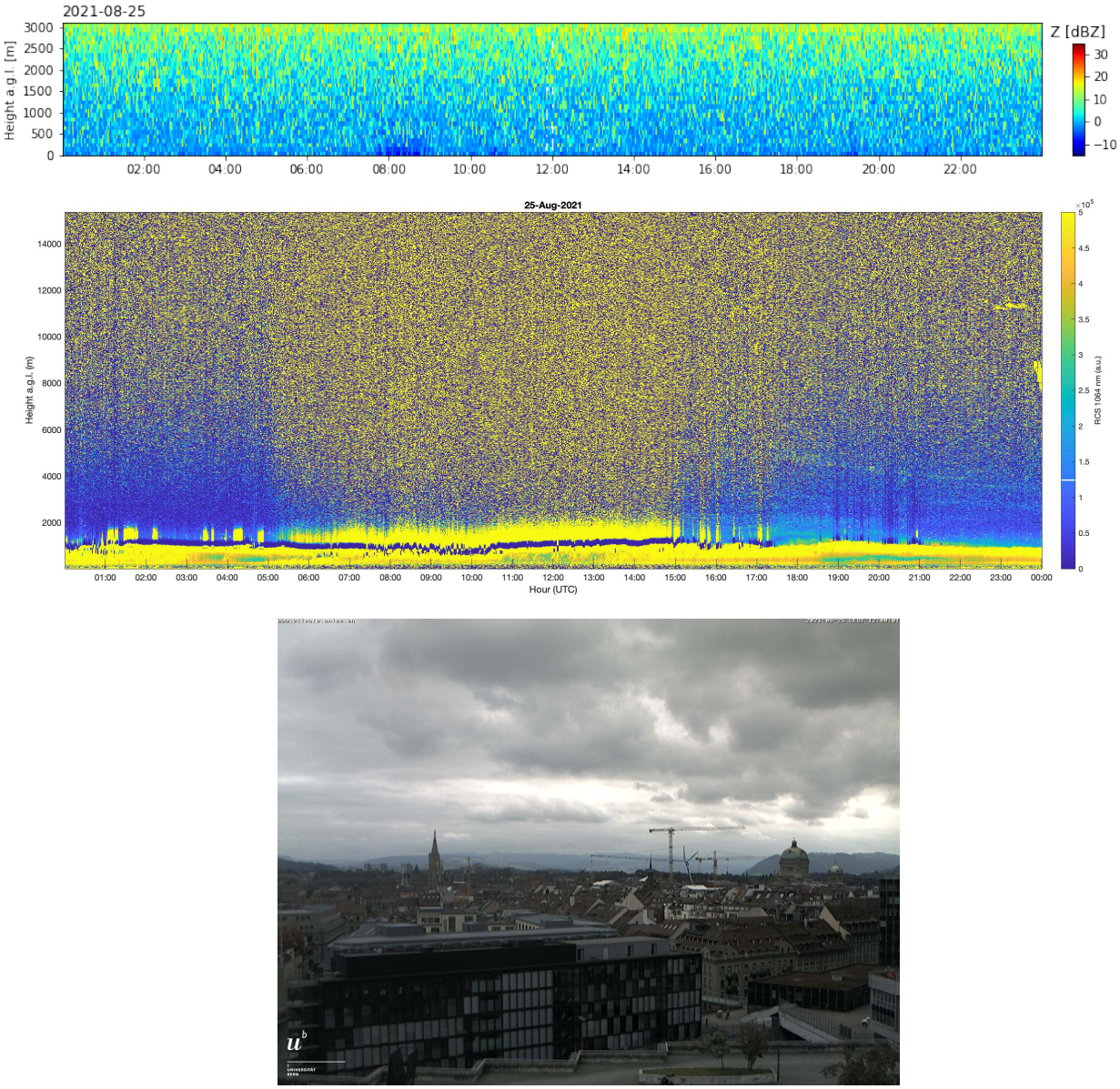

Figure 15. For the 25 August 2021, the ceilometer measurements (RCS - range corrected signal) clearly show that there existed a cloud cover over the weather station,indicated by the dark entries at a height of approximately 1 km throughout the whole period. The webcam image confirms these measurements, showing a uniform cloud cover stretching over the entire visible sky. No significant signal can be detected in the MRR reflectivity, this coincides with the measurements of the ceilometer, on which neither precipitation can be detected.

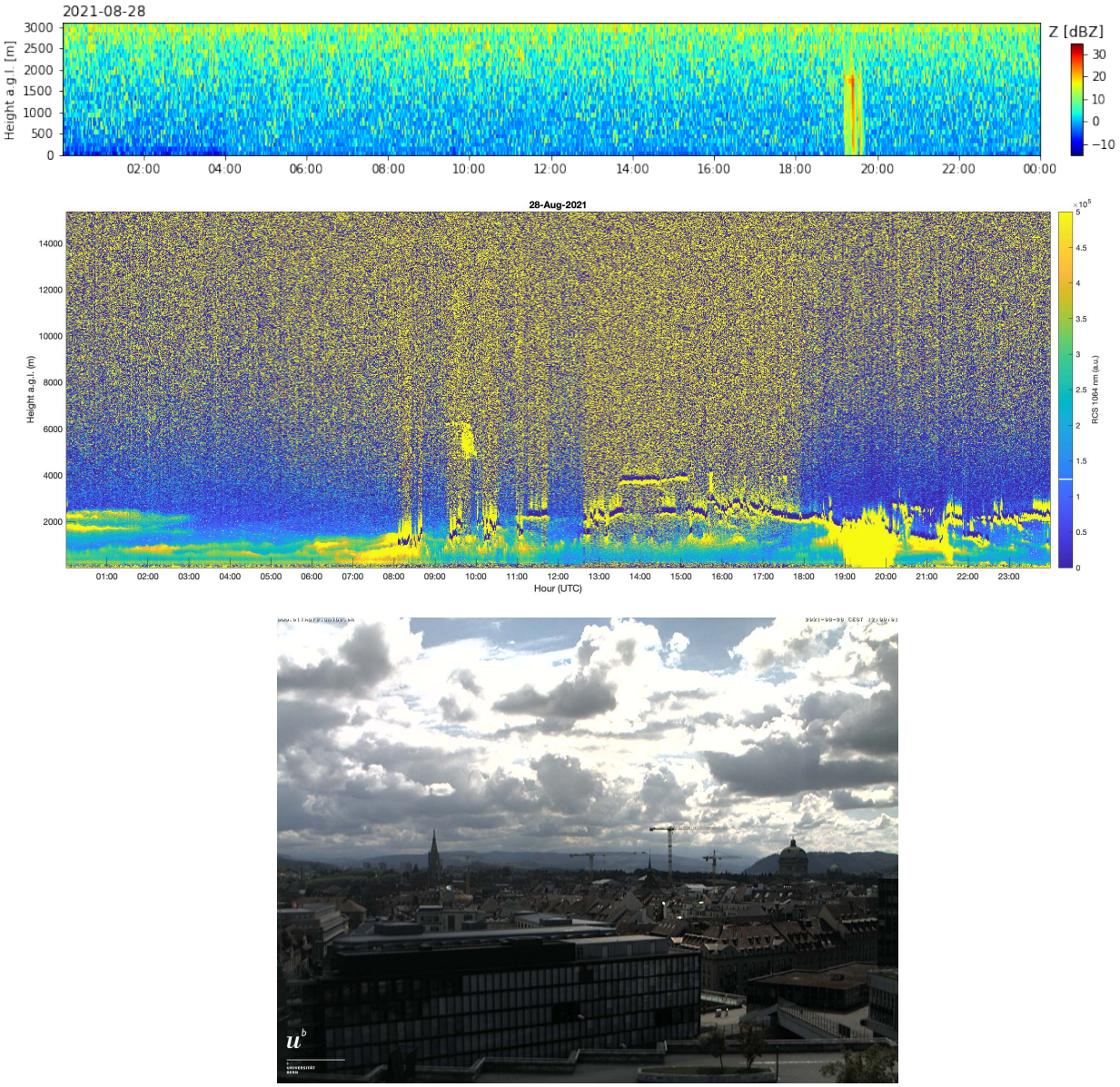

Figure 16. The ceilometer measurements (RCS - range corrected signal) from the 28 August 2021 show that several clouds passed over the weather station at heights between 0.5 and 4.0 km, and were thus partly within range of the radar. Furthermore, it is visible in the measurements that there was a precipitation event between 19:00 and 20:00 UTC, indicated by the increased signal strength near the ground. The webcam image as well displays many individual clouds, but no continuous cloud cover. The reflectivity of the MRR also contains only one event with a strong signal between 19:00 and 20:00 UTC and is thus congruent with the measurements of the ceilometer, but no signal is apparent from the clouds themselves.

7.4 Virga precipitation of 8 April 2008

The first event of virga precipitation that we present in Fig. 17 is from the 8 April 2008. The virga precipitation begins at about 05:30 UTC and ends at the latest with the onset of ground precipitation at about 13:00 UTC. However, the virga phase is not continuous, there are several smaller gaps where no precipitations was detected and therefore no data exists.

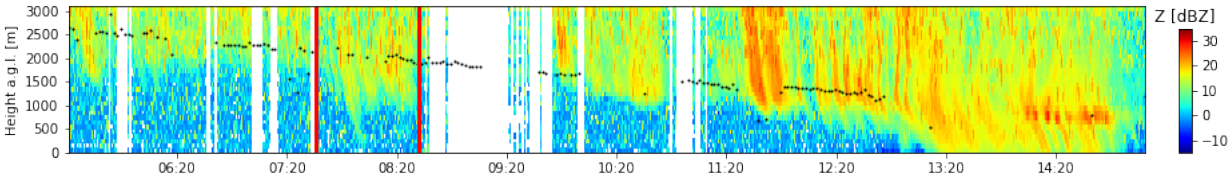

Figure 17. Radar reflectivity of 8 April 2008 from 05:20 to 15:08 UTC using the data processing of Garcia-Benadi et al [6]. The red lines mark the selected virga segment, see Fig. 18. The empty spaces represent missing raw data, presumably due to the conditional recording. The black dots highlight the cloud base detected by the ceilometer.

For the sake of clarity, the other precipitation parameters measured by the MRR are only displayed for a segment of the entire virga event in Fig. 18. In this figure a mask was applied to the parameters, namely to those measured values whose precipitation rate was zero and to those whose reflectivity factor was less than -2 dBZ, which is the minimal detectable reflectivity according to METEK [21]. The displayed segment starts at 07:36 and ends at 08:32 UTC. The reflectivity over the segment duration is very inhomogeneous and consists of stripes of increased reflectivity, whereby their maximum value is rather low at slightly below 25 dBZ. During the period it was possible to measure at times a cloud layer between 1.9 km and 2.2 km above the ground. For the precipitation rate and the characteristic fall velocity, a correlating picture to the reflectivity emerges: non-homogeneous and stripes of increased activity, but no excessive values. Based on the height, the season and the precipitation classification, precipitation can be assumed to be snowfall and wet snow because at that time the 0°-isotherm was located at an altitude of about 1 km, as can be seen in Fig. 19. The maximally occurring precipitation rates of over 3 mm/h are still considered as moderate precipitation. A bright band signal cannot be observed because the precipitation does not completely melt into rain.

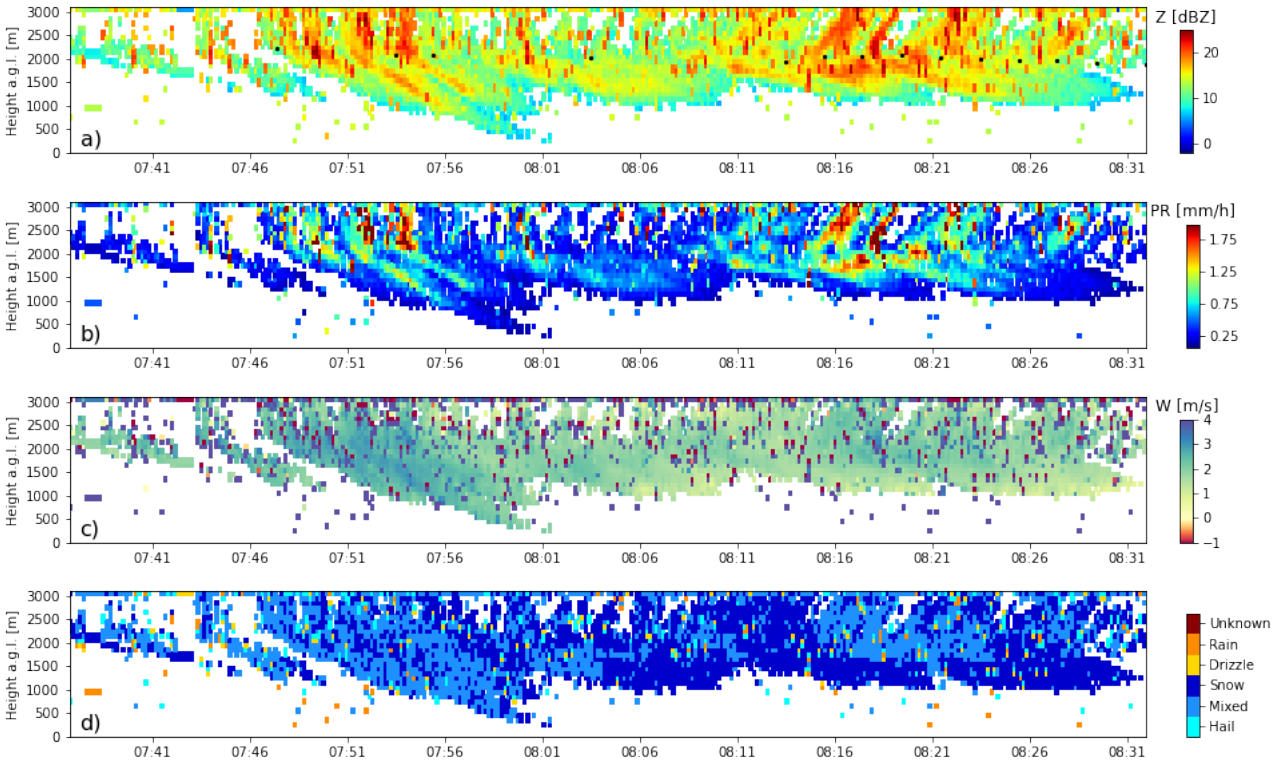

Figure 18. Segment of the virga event that occurred on 8 April 2008. The plots are all derived from MRR measurements using the data processing of Garcia-Benadi et al [6]. (**a**) time-height plot of the reflectivity. (**b**) time-height plot of the precipitation rate. (**c**) time-height plot of the characteristic fall velocity. (**d**) time-height plot of the precipitation type. The cloud base detected by the ceilometer is highlighted by black dots in panel (**a**).

7.4.1 Meteorological situation

The weather services reported for the 8 April 2008, mild but also humid southwesterly winds aloft. In Addition, weak Bise-wind (cold and dry wind) in the region to which the measuring station belongs. In the Alps, a Föhn-wind (dry and warm down-slope wind) was registered coming from the south and lasting until about 10 UTC [26],[22],[23].

This weather forecast is also reflected in the time series of the ERA5 data over Bern (Fig. 19), the temperature profile shows warmer high altitude air and also a clear warming of the temperatures below an altitude of 1 km, which is probably caused by the Föhn-wind. In addition, the updrafts and downdrafts are presented,

but they are quite weak during the virga phase with light downdrafts below an altitude of 0.5 km and light updrafts from an altitude of 2 km upwards. We assume that they are not relevant for the virga precipitation on this scale. In the horizonal wind profiles, a pronounced wind shear is clearly recognisable during the virga phase, especially in the eastward component U. Observing the relative humidity, a stratification into humid and drier air is visible during the virga phase, with drier air near the ground and humid air above.

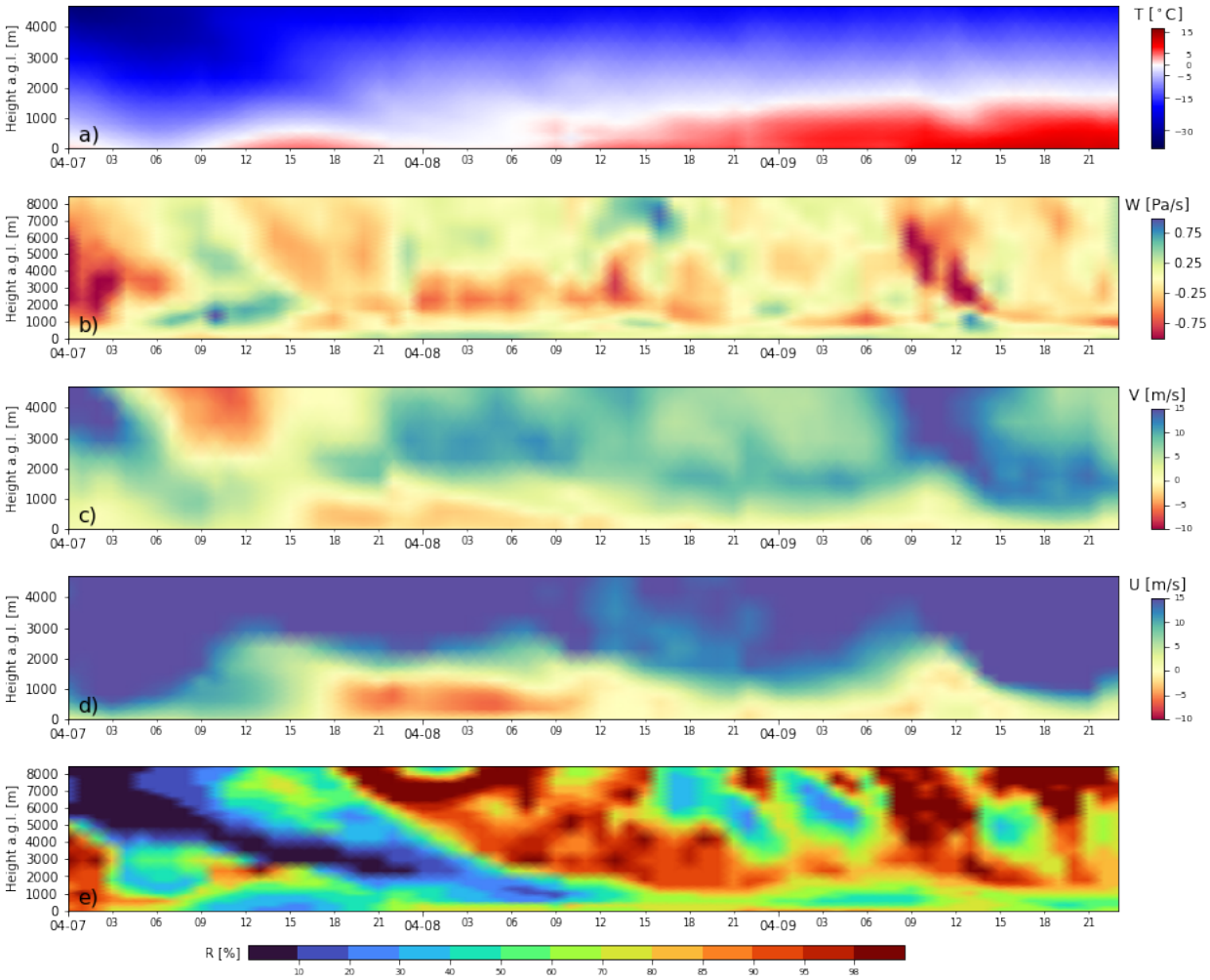

Figure 19. ERA5 data at a grid point close to Bern from 7 April 2008 up to and including 9 April 2008 with a temporal resolution of one hour. (**a**) time-height plot of the temperature. (**b**) time-height plot of the vertical velocity. (**c**) time-height plot of northward component of the wind. (**d**) time-height plot of the eastward component of the wind. (**e**) time-height plot of the relative humidity.

Figure 20 displays ERA5 data from 8 April 2008 at 7 UTC at different altitudes, which is right after the start of the virga precipitation. At an altitude of 700 m a.s.l., a medium-strong wind blows from the northeast towards Bern, bringing cold and medium-humid air with it. At the same time, a weak Föhn-wind blows from the southeast, bringing warm and dry air. At an altitude of 1150 m a.s.l., the wind shifts completely to an easterly direction, with warmer air coming from the south mixing with the cold air from the east, bringing very dry air to the region of Bern. At an altitude of 2900 m a.s.l., the picture is completely different, with a strong southwesterly wind bringing mild but also humid air.

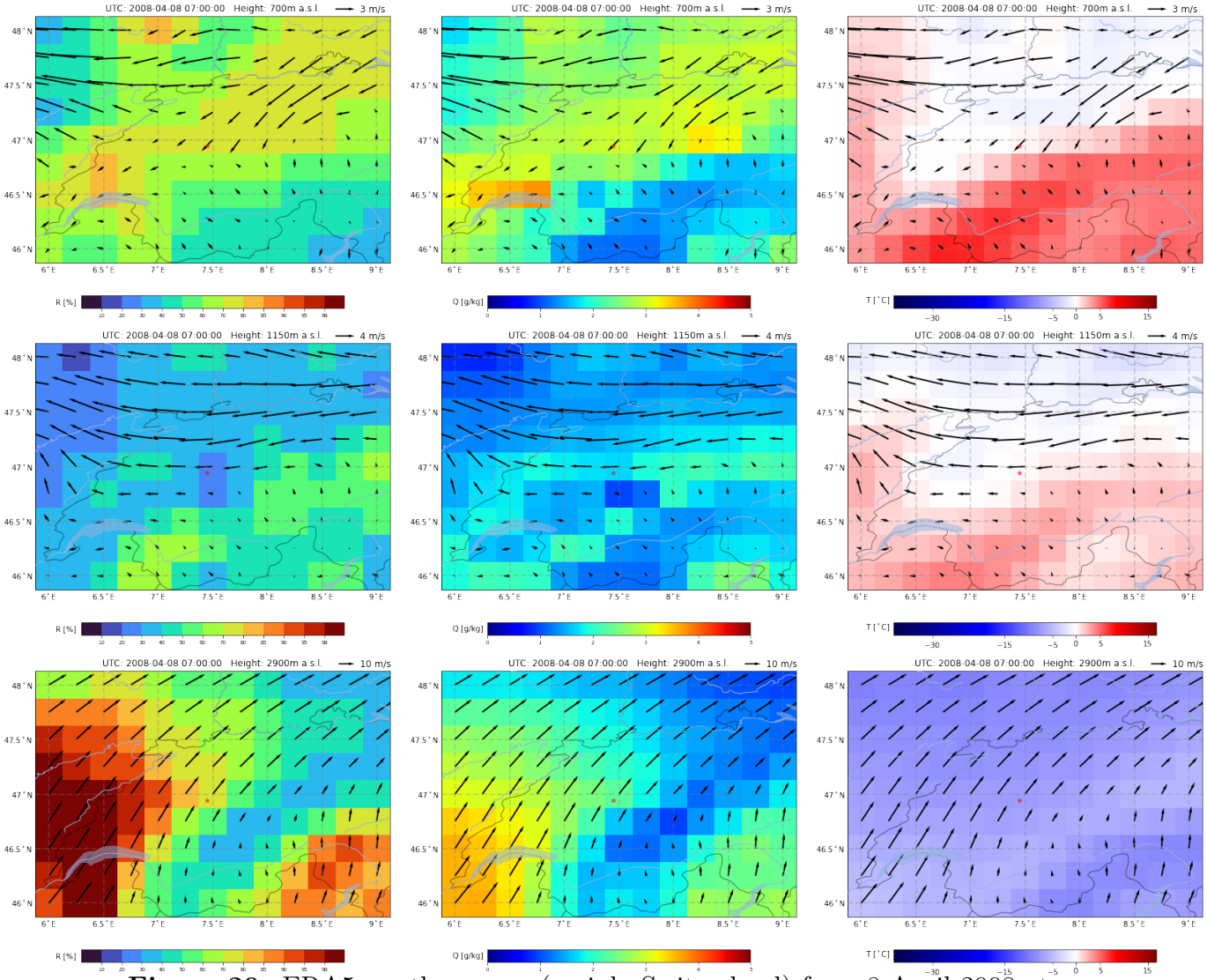

Figure 20. ERA5 weather maps (mainly Switzerland) from 8 April 2008 at 07:00 UTC. Displayed are the relative humidity R, the absolute humidity Q, the temperature T and the horizontal wind speeds at different heights (a.s.l.) with a horizontal resolution of 0.25° x 0.25°. The location of the MRR is marked with a red star in the center.

At 11 UTC (Fig. 21), more towards the end of the virga precipitation, at an altitude of 700 m a.s.l., it becomes apparent that the wind now blows more from a northerly direction, still bringing dry but much warmer air. At an altitude of 1150 m a.s.l., the wind has decreased a bit and shifted to a slightly southeasterly direction, carrying less dry air. At 2900 m a.s.l., a strong southwest wind is still blowing, which has now brought the very humid air over the region of Bern.

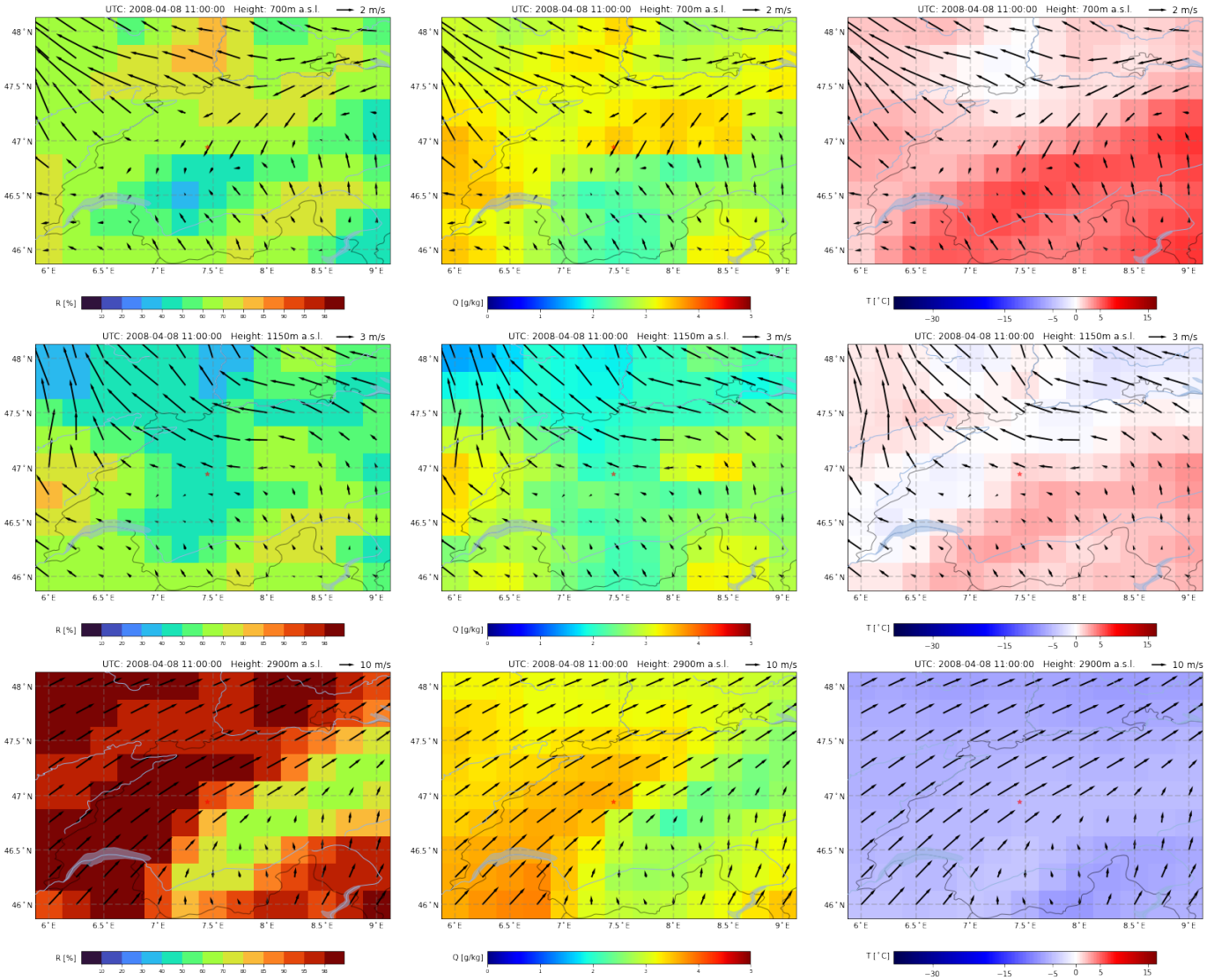

Figure 21. ERA5 weather maps (mainly Switzerland) from 8 April 2008 at 11:00 UTC. Displayed are the relative humidity R, the absolute humidity Q, the temperature T and the horizontal wind speeds at different heights (a.s.l.) with a horizontal resolution of 0.25° x 0.25°. The location of the radar is marked with a red star in the center.

At 14 UTC (Fig. 22), after the end of the virga precipitation and the onset of ground precipitation, a different picture emerges at an altitude of 700 m a.s.l., the winds have completely died down in the region of Bern. At the height of 1150 m a.s.l., the wind shifted to a southerly direction and decreased noticeably. At 2900 m a.s.l., the situation remains unchanged, with southwesterly winds continuing to bring very humid air, which has now spread over the entire map section.

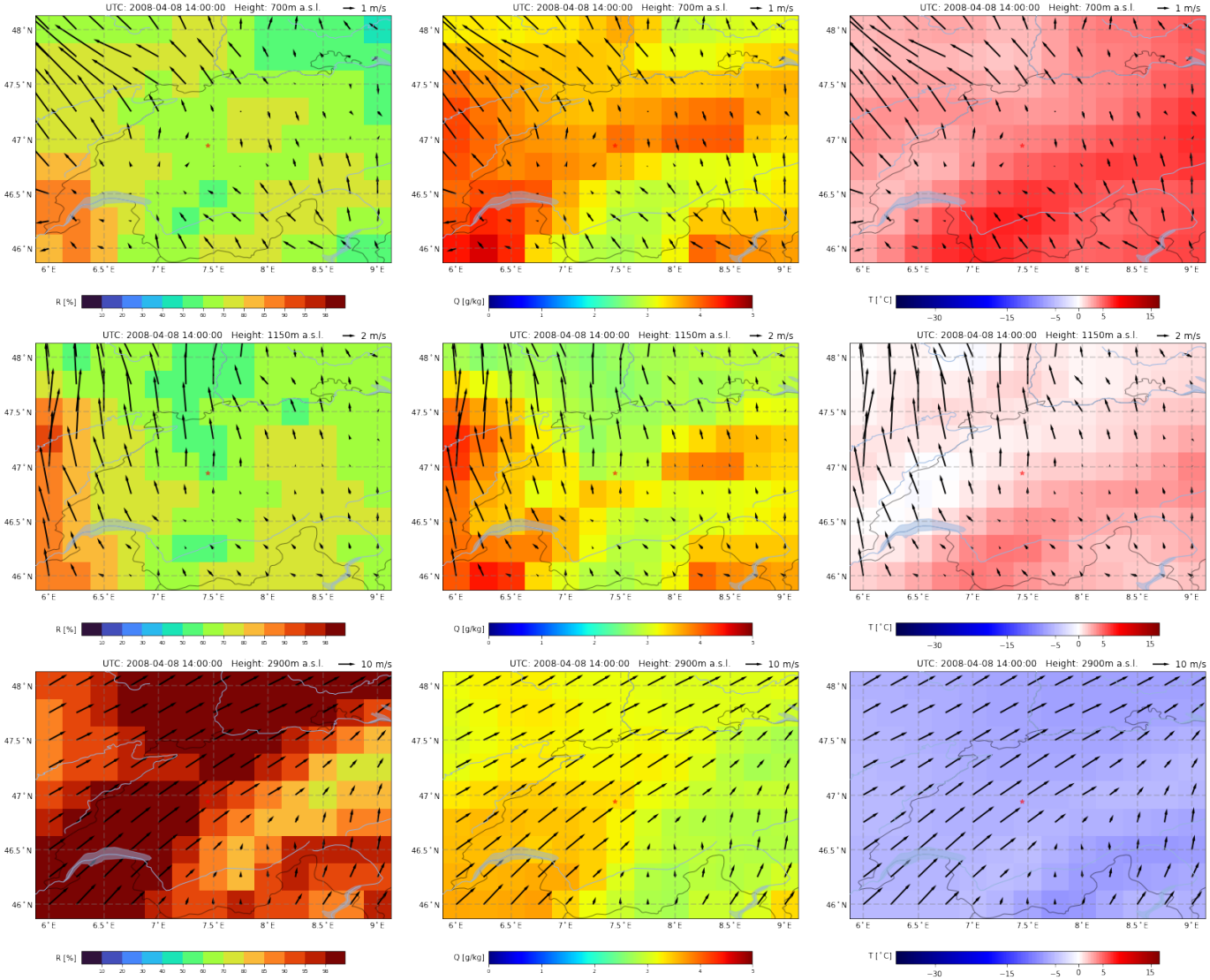

Figure 22. ERA5 weather maps (mainly Switzerland) from 8 April 2008 at 14:00 UTC. Displayed are the relative humidity R, the absolute humidity Q, the temperature T and the horizontal wind speeds at different heights (a.s.l.) with a horizontal resolution of 0.25° x 0.25°. The location of the radar is marked with a red star in the center.

Figure 23 shows the back trajectories calculated with the HYSPLIT model on 8 April at 9 UTC. The back trajectories were calculated for air parcels over Bern at altitudes of 700 m, 1150 m and 2900 m a.s.l., which corresponds to altitudes of 125 m, 575 m and 2325 m above the measuring station (based at 575 m a.s.l.). In the back trajectories it can be seen that the lower air layers of the atmospheric column above Bern originate from high altitudes and because of the lapse rate the descended air is relatively dry. The upper layer of air above Bern, on the other hand, originates from a lower altitude and has risen on its way, which is why its relative humidity is higher.

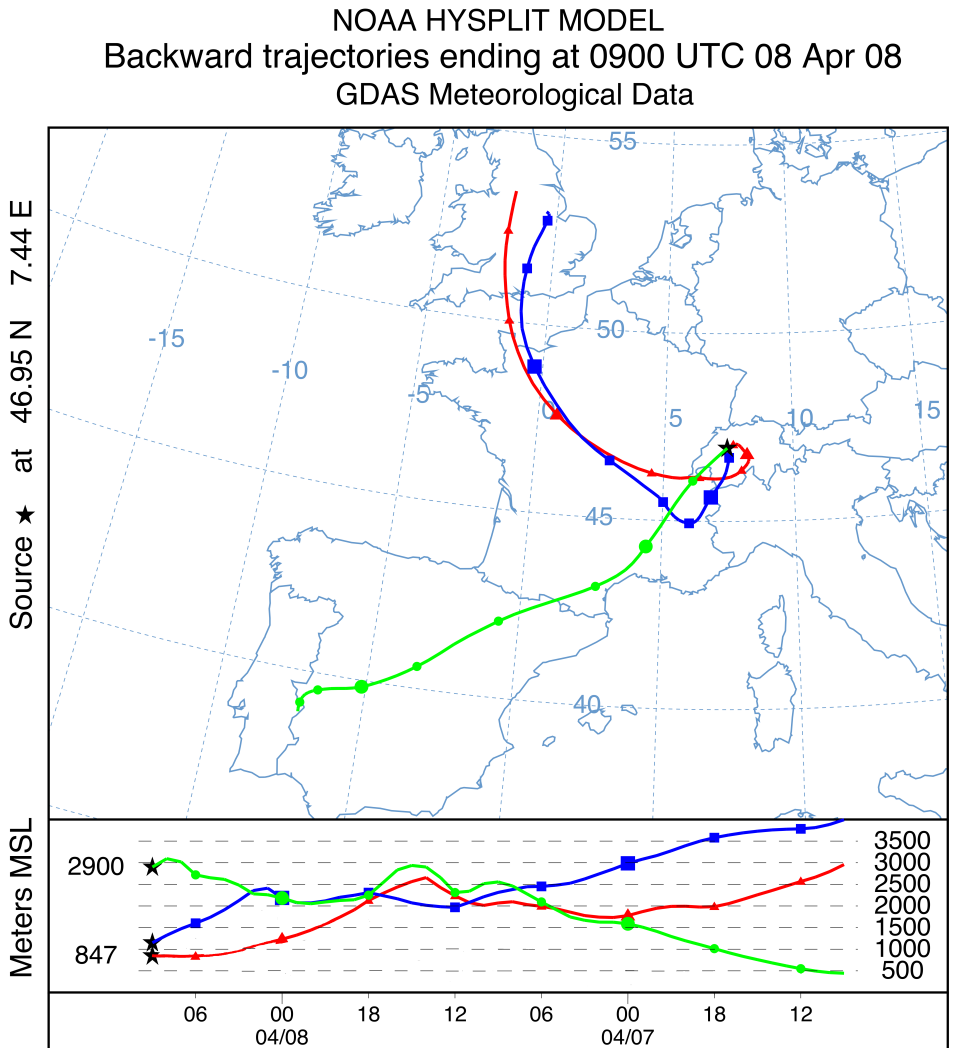

Figure 23. Back trajectories from the 8 April 2008 at 8 UTC for the heights 700 m, 1150 m and 2900 m above sea level. Calculated with the HYSPLIT model (lower panel has a reversed time axis).

Figure 24 shows different precipitation parameters from the ERA5 datasets. These largely agree with the measurements of the MRR. It can be seen in panel (**a**) that there was virga precipitation in the form of snow. Panel (**b**) additionally shows that precipitation reaches the ground in the form of rain from 12 UTC on, although an order of magnitude smaller compared to the snow precipitation. This agrees with the MRR measurements in that precipitation then reaches the ground, but the MRR classifies the precipitation as snow and not as rain (compare with Fig. 37). Panel (**c**) displays precipitation reaching the ground from 12 UTC onwards which agrees with the MRR measurements.

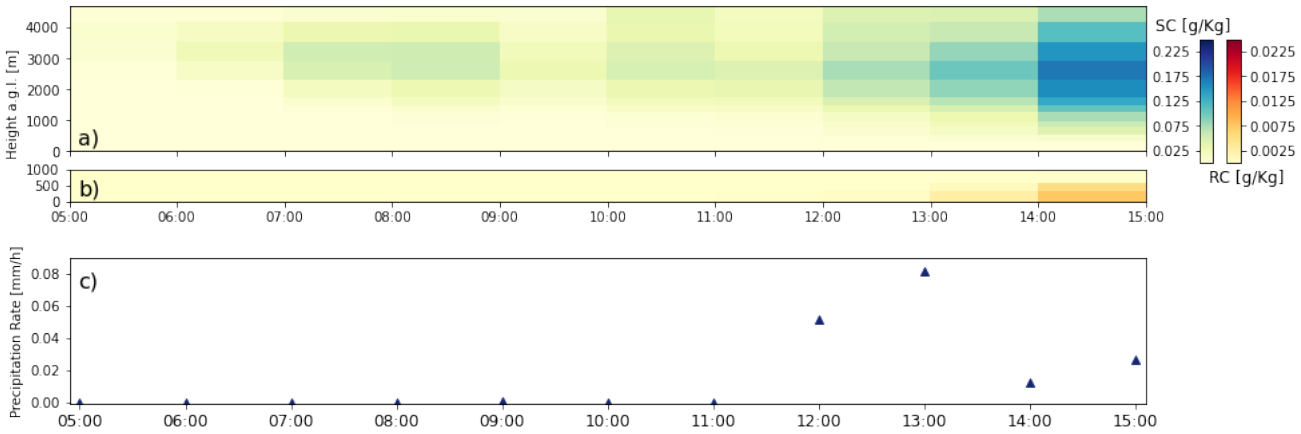

Figure 24. ERA5 data at a grid point close to Bern from 7 April 2008 up to and including 9 April 2008. (**a**) specific snow water content (SC). (**b**) specific rain water content (RC). The specific contents are defined as mass of snow/rain per kilogram of the total mass of moist air. (**c**) total precipitation on the earth's surface given as depth in mm of water equivalent.

7.4.2 Summary

The virga precipitation event presented lasted for roughly eight hours, during which time precipitation in the form of snow or wet snow was measured more or less continuously by the MRR. The lowest altitudes reached by the precipitation before it sublimated or evaporated were usually between 1 km and 1.5 km above the ground. The height at which the precipitation initiated is not known, the MRR has a maximum range of 3 km, but the measurements show that the precipitation mostly originated already higher. The precipitation rates recorded are classified as light to occasionally as moderate with a maximum of 3 mm/h.
The atmospheric reanalysis data from ERA5 reveal that a wind shear prevailed during the virga precipitation phase. In the lower layers (below 1.5 km a.g.l.), unsaturated air reached the measuring station, mostly coming from a southeasterly or northeasterly direction. The back trajectories reveal that these air masses descended from high altitudes. Above this, at higher altitudes, winds from a southwesterly direction carry saturated air over the measuring station from which the precipitation originates. The back trajectories show that these air masses have risen continuously from the surface level.
We suspect that the virga precipitation situation is caused by the wind shear in combination with light precipitation rates. Because unsaturated air is constantly carried into the lower layers by the winds, the precipitation can continuously evaporate or sublimate without the air layer ever becoming saturated. The evaporation or sublimation rate is even fostered by the fact that the precipitation is in the form of snow or wet snow, which has a lower fall velocity than liquid precipitation and thus remains longer in the unsaturated air masses.
Another source for virga precipitation that we could imagine would be strong updrafts. However, we consider this to be rather unlikely, because only very weak updrafts and downdrafts are visible in the atmospheric reanalysis data and local strong vertical winds actually mainly occur in convective precipitation events, which are neither common in this duration nor in this season at the location.

7.5 Virga precipitation of 17 March 2013

The second virga precipitation event that we present in Fig. 25 is from 17 March 2013. One can observe that the virga precipitation started shortly before midnight on the previous day and lasted for a rather long time, ending around 21:30 UTC with the onset of the ground precipitation. But virga precipitation has not been measured continuously, there exist one major and several minor gaps due to the lack of activity.

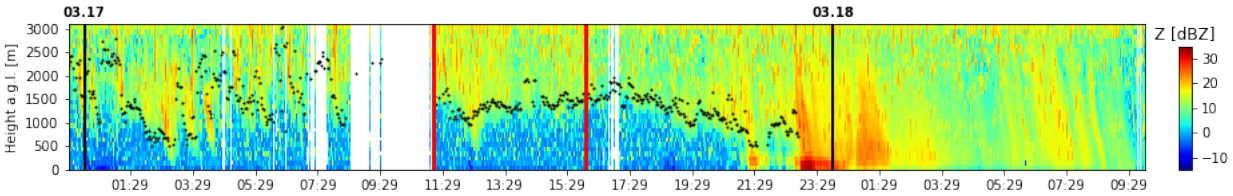

Figure 25. Radar reflectivity from 23:29 UTC of 16 March 2013 until 10:00 UTC of 18 March 2013 using the data processing of Garcia-Benadi et al [6]. The red lines mark the selected virga segment, see Fig. 26. The empty spaces represent missing raw data presumably due to the conditional recording. The black dots highlight the cloud base detected by the ceilometer.

Due to the presentability, the further precipitation parameters measured by the MRR are only presented for a segment of the entire virga event in Fig. 26. A mask was applied to the parameters in this figure, namely to those measured values whose precipitation rate was zero and to those whose reflectivity factor was less than -2 dBZ, which is the minimal detectable reflectivity according to METEK [21]. The recording of the shown segment starts at 11:12 and ends at 16:05 UTC. The reflectivity exhibits varying characteristics, until about 13:30 UTC values above 15 dBz are frequently observed, afterwards the values range generally between 10 and 15 dBz. Over almost the entire period, the ceilometer measured a cloud layer whose lower limit ranged between 1 km and 2 km above the ground. The precipitation rates are quite low and rarely exceed 1 mm/h. The characteristic fall velocities are mostly close to 2 m/s and thus rather in the higher range for snow. As expected for this season and the altitude of the precipitation, it consists mostly of snow according to the classification, with the occasional occurrence of wet snow. As expected, a bright band signal is not present as precipitation only occurs in the form of snow above the 0°-isotherm.

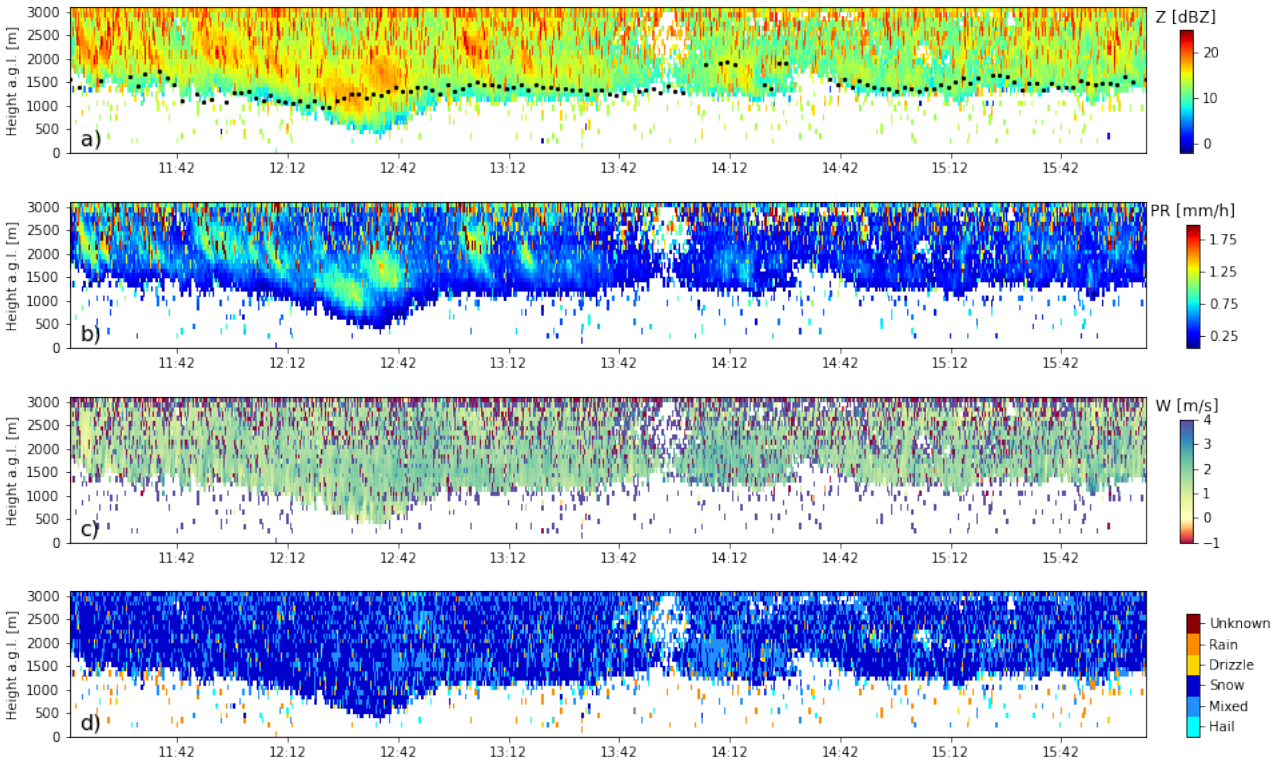

Figure 26. Segment of the virga event that occured on 17 March 2013. The plots are all derived from MRR measurements using the data processing of Garcia-Benadi et al [6]. (**a**) time-height plot of the reflectivity. (**b**) time-height plot of the precipitation rate. (**c**) time-height plot of the characteristic fall velocity. (**d**) time-height plot of the precipitation type. The cloud base detected by the ceilometer is highlighted by black dots in panel (**a**).

7.5.1 Meteorological situation

On 17 March 2013, the weather service reported stormy Föhn-wind (dry and warm down-slope wind) over the Alps and clouds at higher altitudes approaching from a southwesterly direction [24],[25].

Let's look at the time series of the ERA5 data over Bern (Fig. 27). The temperature profile shows at an altitude below 1 km an increased temperatures during the virga phase, which is probably due to the Föhn-wind. The updrafts and downdrafts are not very pronounced during the virga phase. Below an altitude of 1 km weak downdrafts can be observed, which probably originate from the precipitation. But near the ground there are then again very weak updrafts and from an altitude

of 1.5 km on, light updrafts can be found again. In the horizontal wind profiles a wind shear is visible in the eastward component U during the virga phase, where the shear line is located at an altitude of around 1.5 km. The relative humidity profile shows that during the entire virga phase the air below an altitude of 1 km was quite dry, whereas the air above was very humid.

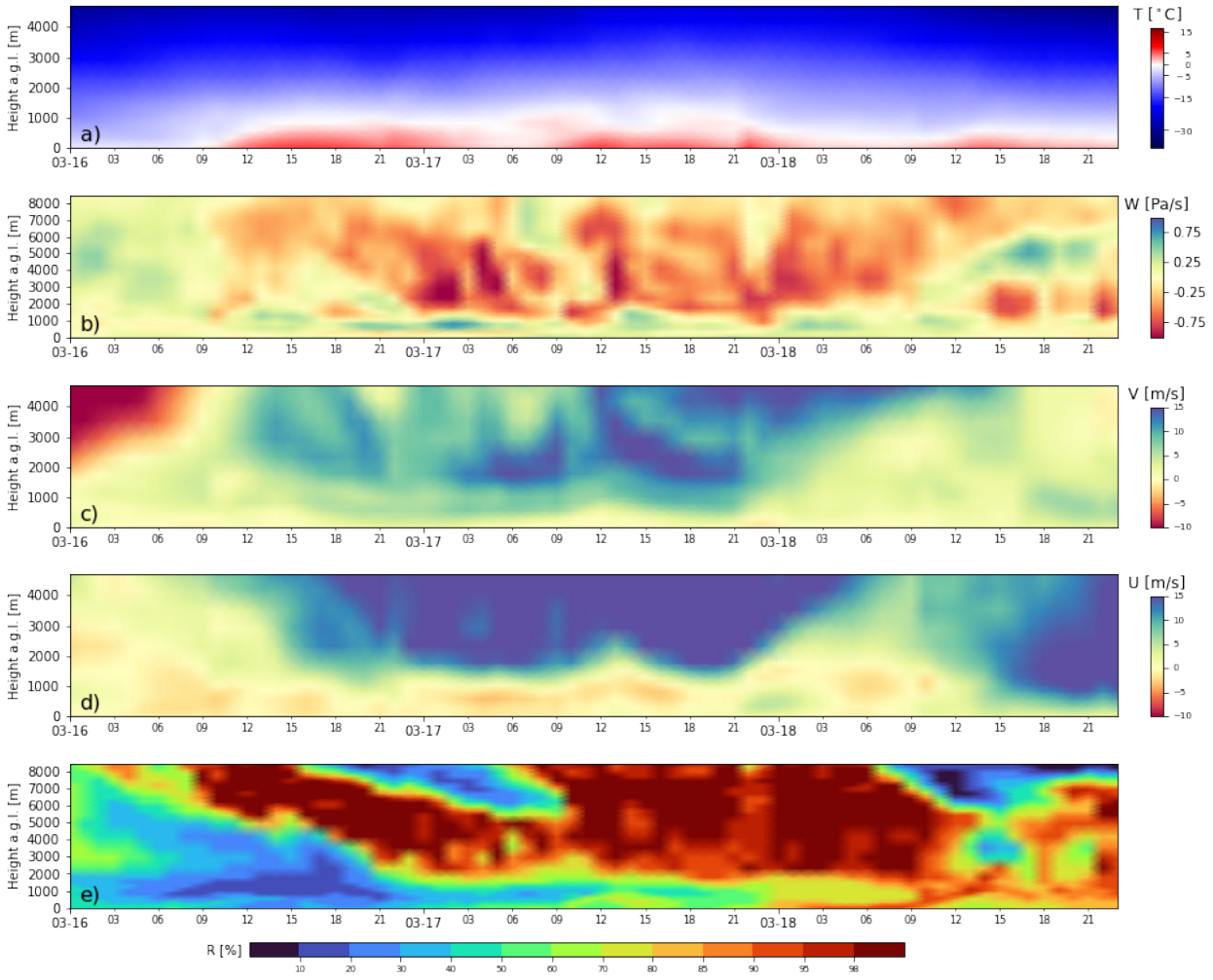

Figure 27. ERA5 data at a grid point close to Bern from 16 March 2013 up to and including 18 March 2013 with a temporal resolution of one hour. (**a**) time-height plot of the temperature. (**b**) time-height plot of the vertical velocity. (**c**) time-height plot of northward component of the wind. (**d**) time-height plot of the eastward component of the wind. (**e**) time-height plot of the relative humidity.

Figure 28 shows ERA5 data from the 16 March 2013 at 23 UTC on different altitudes, which is just before the MRR started registering virga precipitation. At an altitude of 700 m a.s.l., the Föhn-wind coming from the southeast is visible, which moves over the region of Bern, taking warm and dry air with it. A little higher, at 1150 m a.s.l., the wind blows a little bit more from the south and at a faster speed, but it carries equally warm and dry air. At 2900 m a.s.l., a strong wind coming from the southwest is blowing over the region of Bern, bringing humid air with it.

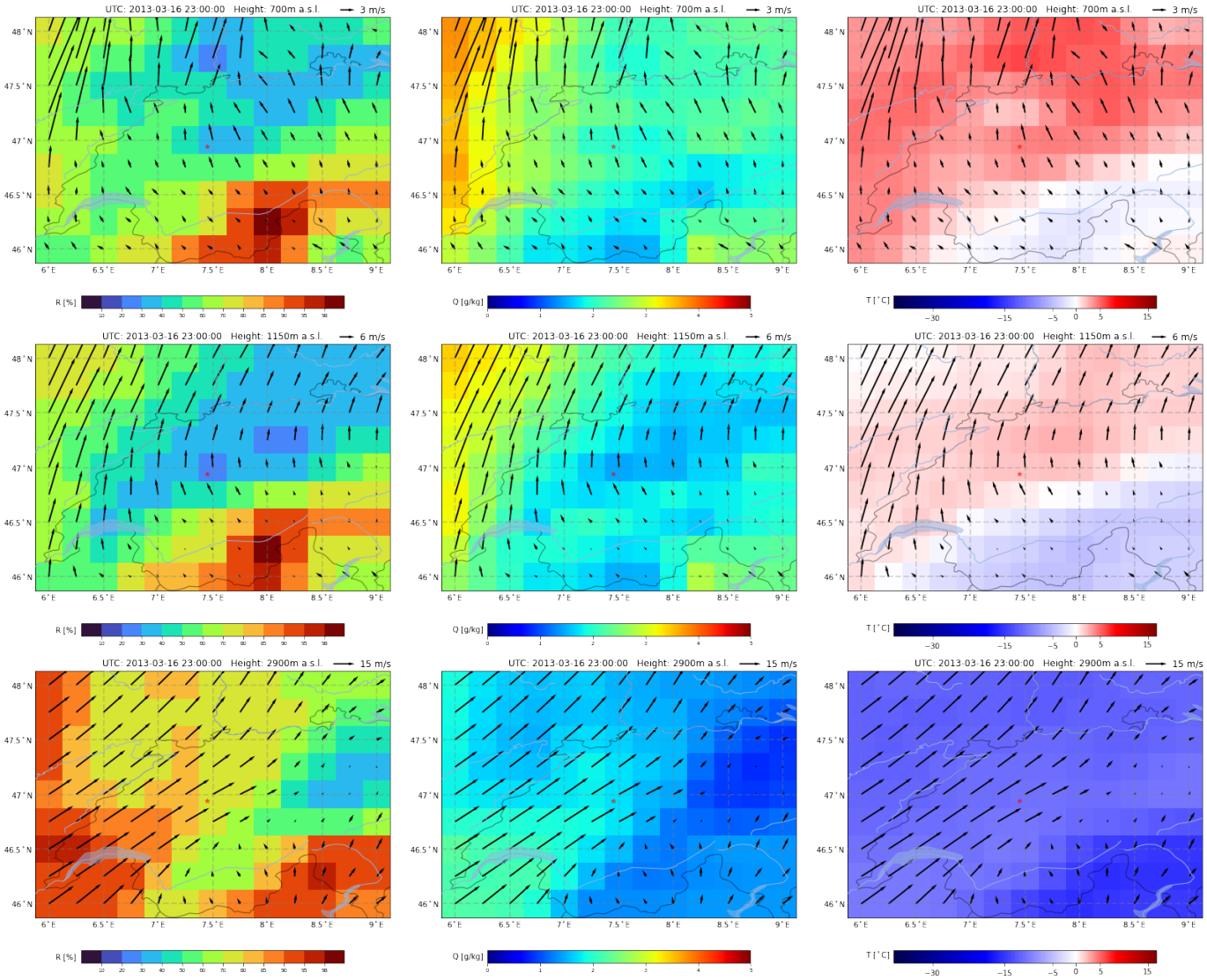

Figure 28. ERA5 weather maps (mainly Switzerland) from 16 March 2013 at 23:00 UTC. Displayed are the relative humidity R, the absolute humidity Q, the temperature T and the horizontal wind speeds at different heights (a.s.l.) with a horizontal resolution of 0.25° x 0.25°. The location of the MRR is marked with a red star in the center.

At 12 UTC the next day (Fig. 29), the Föhn wind is still blowing from a southern direction, but in the region of Bern it has come to a complete standstill at 700 m a.s.l. Above this at a height of 1150 m a.s.l. the wind has lost some of its strength, but it still keeps the relative humidity low at this altitude by bringing in dry air from the south. At 2900 m a.s.l., a southwesterly wind is still blowing, but the humid air tends to pass north of Bern, nevertheless the air in this region is also already more humid.

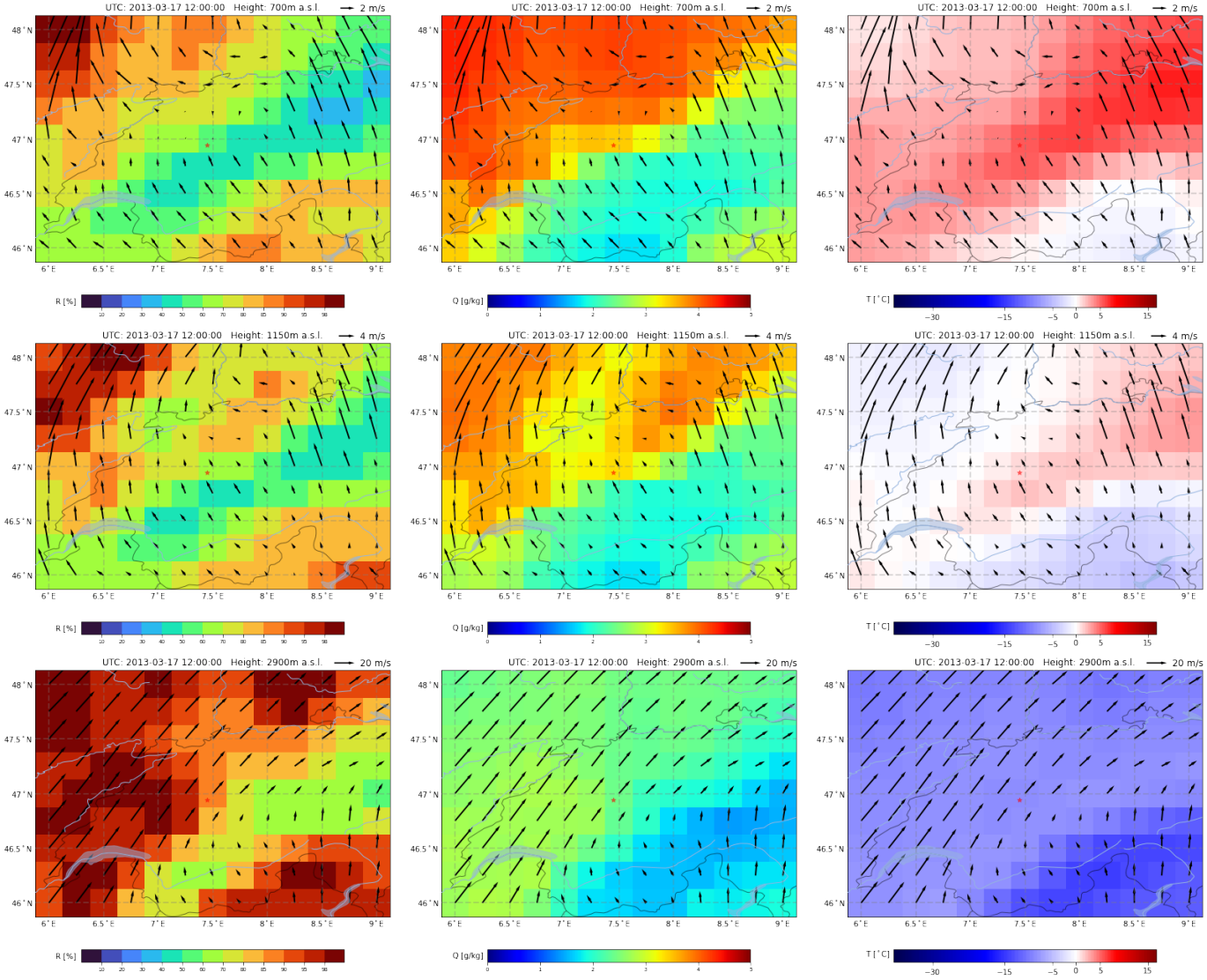

Figure 29. ERA5 weather maps (mainly Switzerland) from 17 March 2013 at 12:00 UTC. Displayed are the relative humidity R, the absolute humidity Q, the temperature T and the horizontal wind speeds at different heights (a.s.l.) with a horizontal resolution of 0.25° x 0.25°. The location of the MRR is marked with a red star in the center.

At 23 UTC on 17 March, shortly after the first precipitation reached the ground, at an altitude of 700 m a.s.l., it can be seen that the wind at this altitude has now also turned in a southwesterly direction, bringing moist air with it. At 1150 m a.s.l., the picture is similar, the southerly wind has almost completely broken down and a humid wind from the southwest is now blowing into the region of Bern. Aloft at 2900 m a.s.l., the wind has lost some of its strength, but it still blows quite strongly and continues to carry moisture with it.

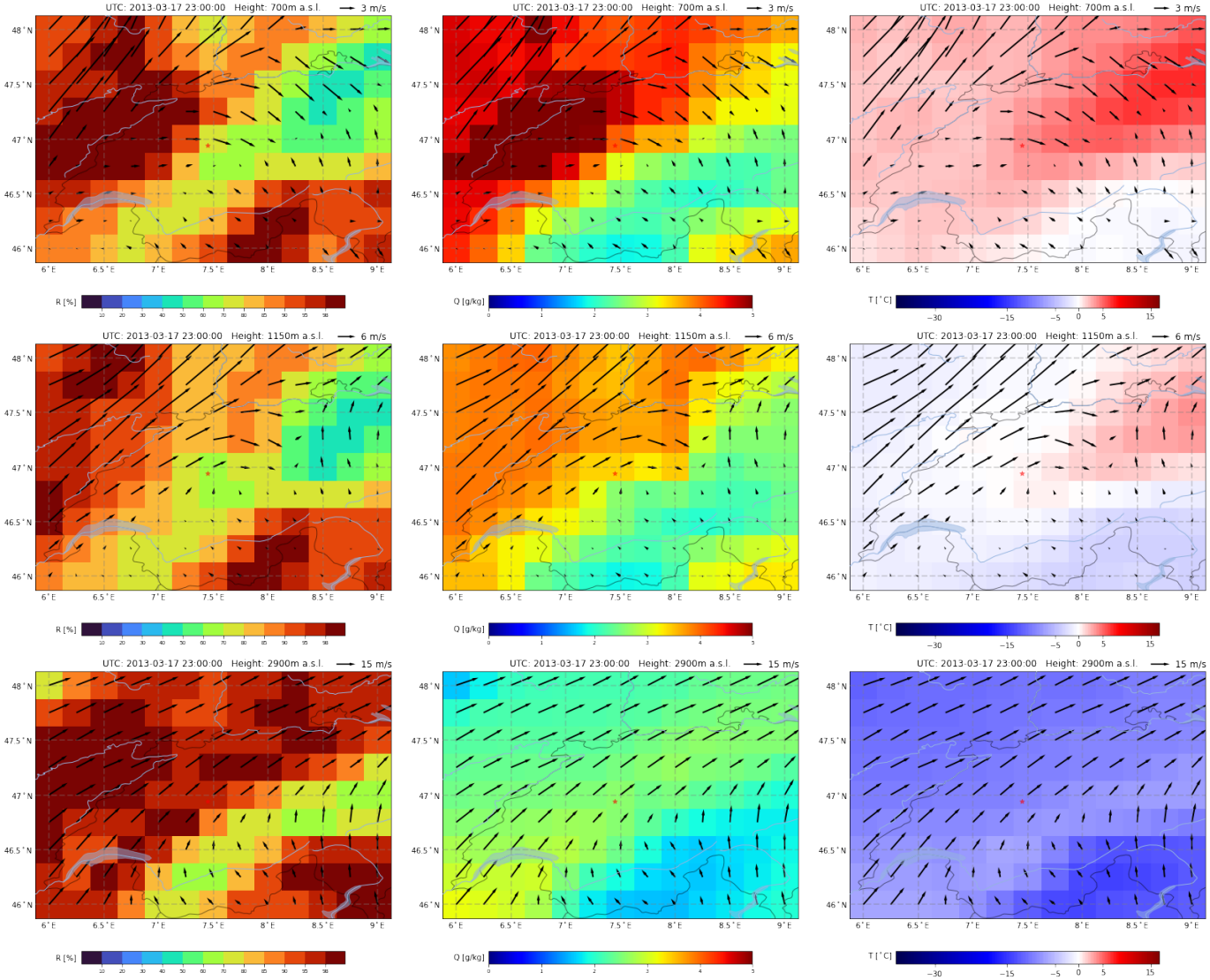

Figure 30. ERA5 weather maps (mainly Switzerland) from 17 March 2013 at 23:00 UTC. Displayed are the relative humidity R, the absolute humidity Q, the temperature T and the horizontal wind speeds at different heights (a.s.l.) with a horizontal resolution of 0.25° x 0.25°. The location of the MRR is marked with a red star in the center.

Figure 31 shows the back trajectories calculated with the HYSPLIT model on 17 March at 13 UTC. The back trajectories were calculated for air parcels over Bern at altitudes of 700 m, 1150 m and 2900 m a.s.l., which corresponds to altitudes of 125 m, 575 m and 2325 m above the measuring station (based at 575 m a.s.l.). It can be seen that the lower air layers of the atmospheric column above Bern originate from northern Europe. They first crossed the Alps in a southerly direction at high altitude, before descending to ground level. They then crossed the Alps again in a northerly direction, but at ground level, arriving in the region of Bern as a dry warm Föhn-wind. The upper air layer above Bern is humid air originating from the Mediterranean region that is in the process of rising. On its way to the region of Bern, it did not pass directly over the Alps but only over their extensions.

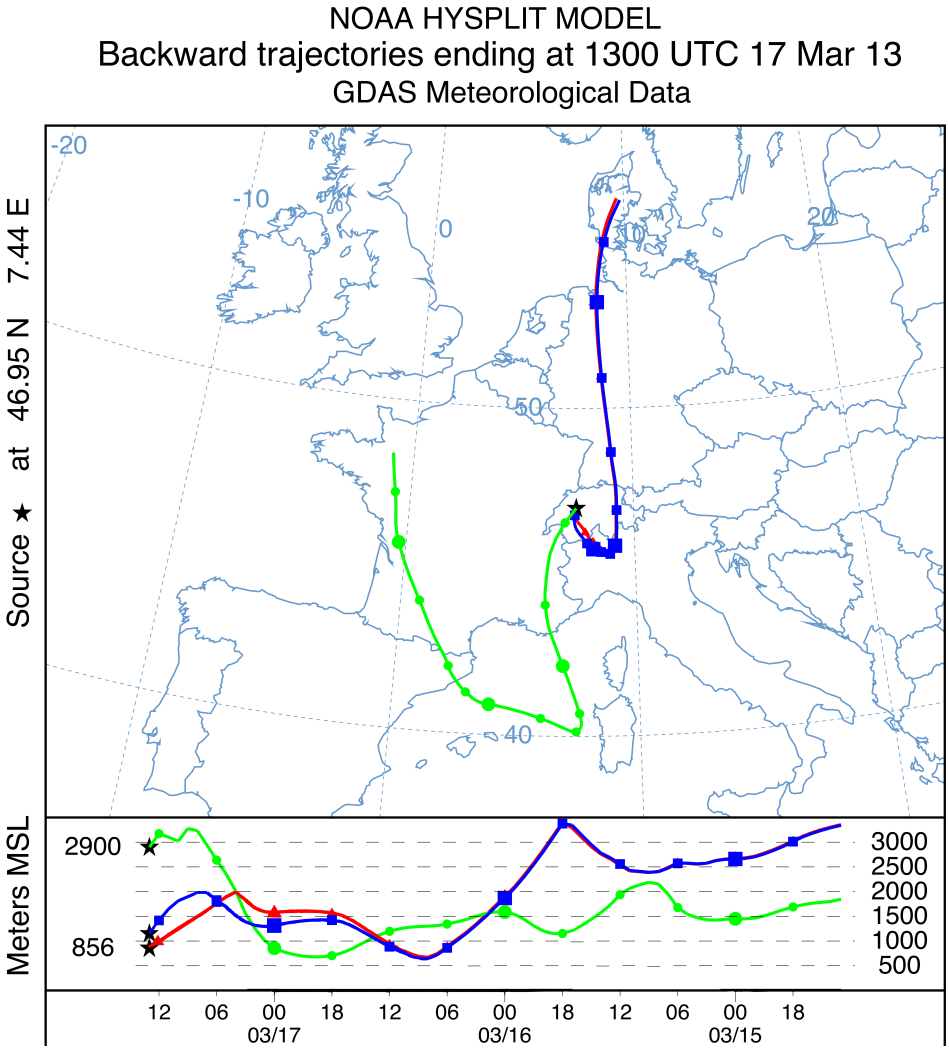

Figure 31. Back trajectories from the 17 March 2013 at 13 UTC for the heights 700 m, 1150 m and 2900 m above sea level. Calculated with the HYSPLIT model (lower panel has a reversed time axis).

Figure 32 shows different precipitation parameters from the ERA5 datasets. These are only partially consistent with the MRR measurements. Panel (**a**) shows that there was virga precipitation in the form of snow, which reaches the ground at about 23 UTC. However, the MRR measurements showed that the precipitation reached the ground somewhat earlier at 21:30 UTC (compare with Fig. 25). In panel (**b**) it can be seen that from 14 UTC onwards precipitation reached the ground in the form of rain. This is not consistent with the measurements of the MRR, which neither recorded ground precipitation at these times nor precipitation in the form of rain. Panel (**c**) displays the precipitation reaching the ground, striking are the precipitation rates at around 6 UTC, which neither match the values in panel (**b**) nor the MRR measurements.

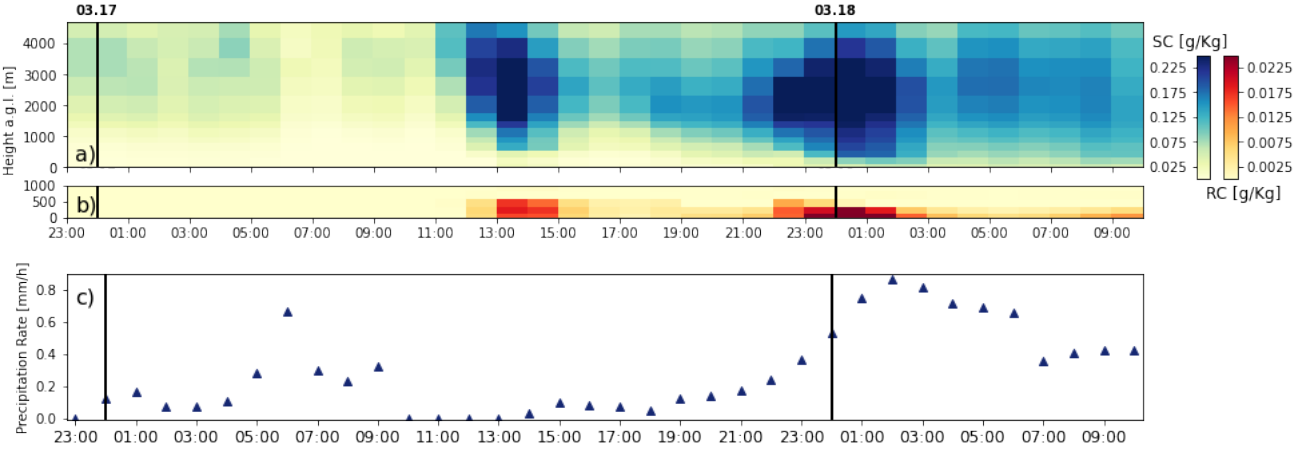

Figure 32. ERA5 data at a grid point close to Bern from 16 March 2013 up to and including 18 March 2013. (**a**) specific snow water content (SC). (**b**) specific rain water content (RC). The specific contents are defined as mass of snow/rain per kilogram of the total mass of moist air. (**c**) total precipitation on the earth's surface given as depth in mm of water equivalent.

7.5.2 Summary

The virga precipitation event shown lasted for about twenty-two hours, during which more or less continuous precipitation was measured by the MRR. The precipitation measured occurred mainly in the form of snow and partly as wet snow. The lowest altitudes reached by the precipitation varied between 300 m and 1500 m before it evaporated or sublimated completely. The measurements do not reveal the maximum height at which altitude the precipitation set in, meaning that most of it started above the maximum height of 3 km which can be resolved by the radar. Most of the precipitation rates recorded were below 1 mm/h and therefore classified as light precipitation but when the precipitation became more intense at times, the precipitation rates were more around 1.5 mm/h, which can still be classified as moderate.
A look at the atmospheric reanalysis data from ERA5 reveals that a wind shear existed throughout the entire duration of the virga precipitation, with the shear line mostly at an altitude of approximately 1.5 km. Below the shear line, the prevailing Föhn-wind carried unsaturated air from a southeasterly direction into the region of Bern. Meanwhile, above the shear line, there was a pronounced wind coming from the southwest, bringing with it both moist and saturated air. The back trajectories show that the air masses in the higher layers above Bern have risen from ground level and have a high humidity. In contrast, the air in the lower layers originates from the north and has fallen from high altitudes and has a low humidity.
Similarly to the first presented virga precipitation event, we suspect that the virga precipitation situation was caused by the combination of a wind shear with low precipitation rates. The wind shear leads to dry air in the lower layers above Bern, guaranteeing the continuous and complete evaporation or sublimation of precipitation from the upper layers above Bern. This is supported by the observation that the precipitation reaches the ground as soon as the southeasterly coming wind breaks off and thereby ends the wind shear.
Also in this event, the updrafts are not pronounced enough for us to assume that they could have a sufficiently strong influence on the precipitation to prevent it from reaching the ground or to significantly extend its fall time.

CHAPTER 8

Conclusions

This study employs vertically aligned K-band Doppler radar observations to identify virga precipitation events in Bern, Switzerland. A new radar data processing by Garcia-Benardi et al. was implemented which allows the detection of snow virga precipitation. Among these, two events were selected, presented and reviewed using atmospheric reanalysis data from ERA5 and atmospheric back trajectories generated by HYSPLIT.
Virga precipitation can occur in a variety of forms and circumstances, however the two cases studied here are alike in many respects. During both events, the MRR was able to record virga precipitation with minor interruptions over several hours, whereby this was composed of snow or wet snow. Both occurred during the meteorological spring and we would like to note that snowfall is not uncommon at this season [27]. Precipitation rates could always be classified as light or moderate at most.
For both events, we assume that the virga precipitation was caused by a prevailing wind shear, whereby moisture-saturated air was carried over the measuring station in the upper air layers while a Föhn-wind or Bise-wind blew in the lower air layers, which continuously carried unsaturated air with it.
Comparable virga precipitation events have been observed and studied by Jullien et al. [13] at Dumont d'Urville station, East Antarctica. Their composite analysis revealed that virga precipitation occurs when precipitating clouds are coming from the sea and simultaneously a low-level katabatic wind (dry fall wind) is blowing from the inland. This also leads to a wind shear, where air with low relative humidity is carried into the lower air layers.
Further evidence for our assumption that virga precipitation can be caused by low-level dry winds is that in the example events discussed it is visible that the wind shear dissipated when the precipitation reached the ground.

During our studies we also found further virga precipitation events, which are not presented in this paper because they were only of short duration and therefore we could not compare them with the reanalysis data and the back trajectories because their spatial and temporal resolution is too coarse. It would be exciting to investigate these cases further, but this would require better resolved reanalysis data,

own numerical atmospheric simulations or supporting equipment for future cases. Such a study would allow one to investigate a possible correlation between strong updrafts and virga precipitation, which is often related to convective precipitation, but which occurs only for a short time in a small region. Furthermore, the relation of virga precipitation and microbursts could be studied.
Other interesting studies would include the frequency and severity of virga precipitation, for which a complete time series of measurements would be required or the micro-physical characteristics which require the uncertainties on the measured parameters to be known, but which we are not aware of.
These further studies could provide deeper insights into the mechanisms and effects of virga precipitation on the radiative transfer and the hydrologic cycle. Moreover, their prediction could become of importance to aviation, because the associated micro-bursts represent a not inconsiderable source of danger for it.

Appendix

The appendix is mainly intended for people who will be working on virga precipitation at the IAP in the future. On the one hand, it contains a further evaluation of precipitation events measured by the MRR and other virga precipitation events that were not investigated further.

Event duration

Figure 33 shows the duration and the precipitation amounts of the identified events n for the years 2008, 2009 and 2010, measured by the MRR at an altitude of 0 - 100m. A precipitation event was defined on the basis of precipitation intensity and separation time as follows: The precipitation intensities must be greater than 0 mm/h at an altitude of 0 - 300 m for each time step considered, and the precipitation sum must be greater than 0.1 mm over the duration of the corresponding event, in addition the total duration must be greater than 1 min. Precipitation events with a threshold value of more than 20 minutes without precipitation were separated.

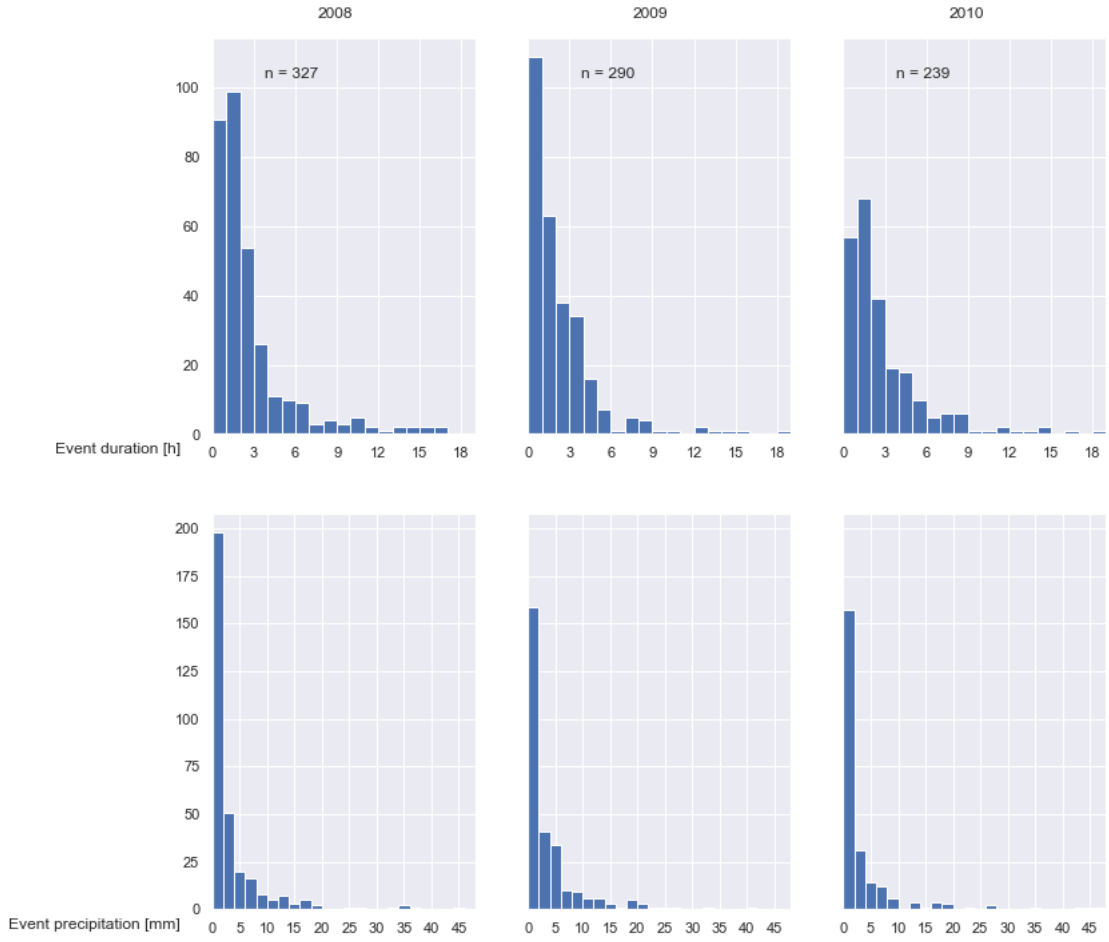

Figure 33. Duration and precipitation amounts of identified events

Figure 34 shows the precipitation sum as a function of event duration over the years 2008, 2009 and 2010.

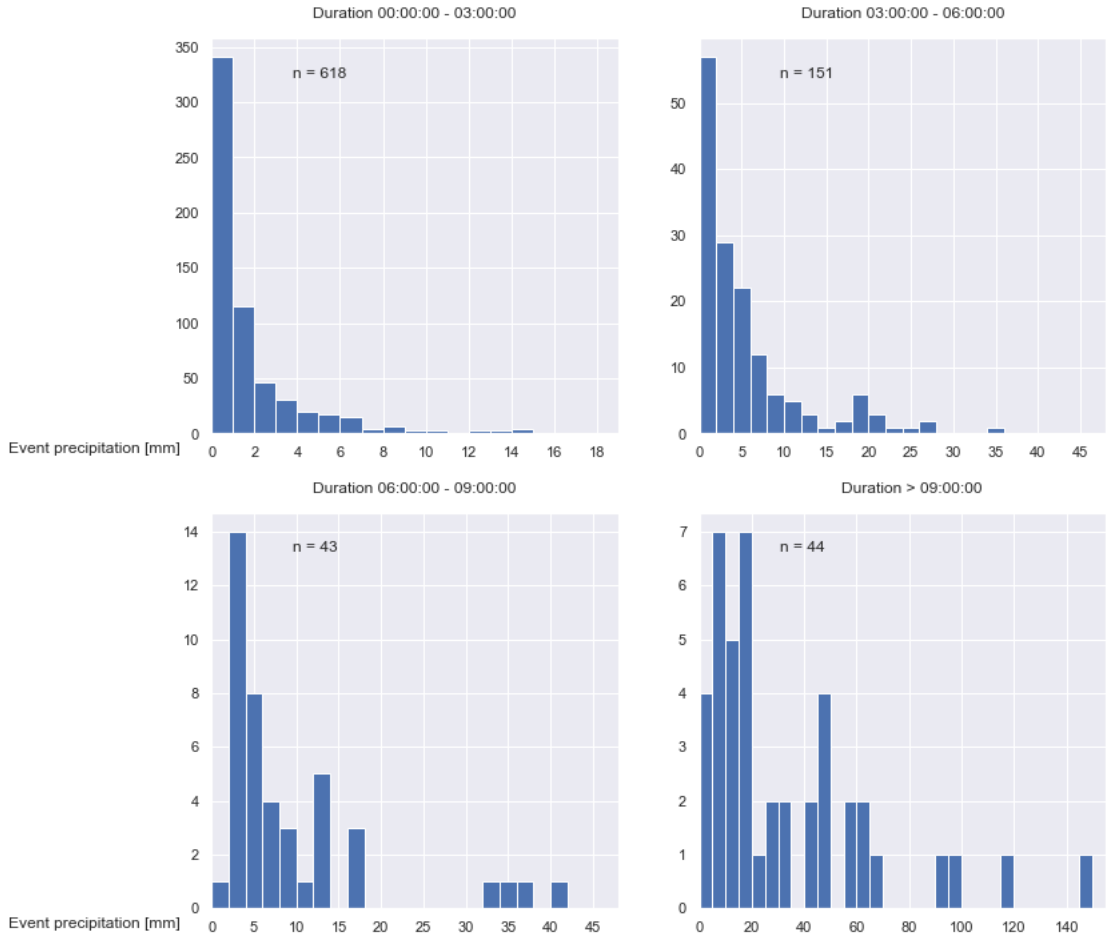

Figure 34. Precipitation sum of events as a function of their duration

Figure 35 shows the duration and the precipitation amounts of the identified events n for the years 2008, 2009 and 2010, measured by the MRR at an altitude of 0 - 100m (**a**) and by the tipping bucket located at the Bollwerk (**b**). Although the tipping bucket on the ExWi building would have been more suitable for comparison, the MRR data were compared with the data from the tipping bucket on the Bollwerk, as the data from the ExWi tipping bucket show a gap of roughly 4 months.

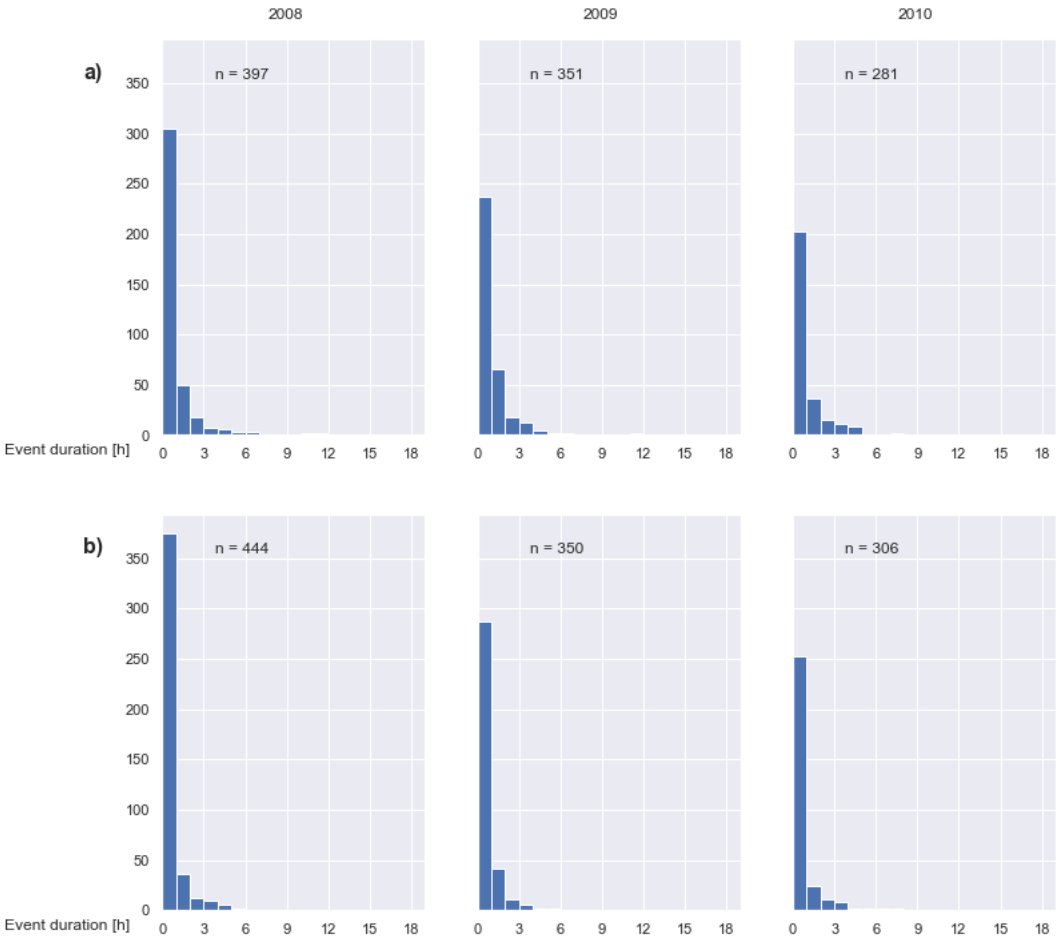

Figure 35. Precipitation sum of the events as a function of their duration, based on the data of the MRR (**a**) and the tipping bucket at Bollwerk (**b**)

In order to be able to compare the data records of the two measuring devices, the MRR data for the Figure 35 was averaged over 10 minutes. In addition, an event for Figure 35 was defined differently than in Figure 33 to take account of the different measuring methods. A precipitation event was defined on the basis of

precipitation intensity and separation time as follows: The precipitation intensities must be greater than 0.1 mm/h for each time step considered, and the precipitation sum must be greater than 0.2 mm over the duration of the corresponding event, in addition precipitation events with a threshold value of more than 30 minutes without precipitation were separated.

Bright Band

The melting layer is the height interval in which the hydrometeors of precipitation change from the solid to the liquid phase, it begins at about the height of the isothermal 0 °C layer. The vertical extent of the melting layer can reach several hundred meters, depending on the parameters influencing the phase transition, such as the lapse rate, the humidity and the precipitation rate. In radar measurements, the melting layer is perfectly visible due to an acceleration of the falling hydrometeors and a higher reflectivity, which is why it is visible on measurements as a bright band. The increased reflectivity can be explained by the observation that when ice crystals pass through the layers with temperatures from -5 to 0 °C, they continue to grow due to the aggregation of other crystals, resulting in larger particles. As these ice crystals sink into the isothermal 0 °C layer, they warm up and become wet. Initially, the ice surface of the crystals will be covered with a thin layer of melted water. However, water reflects the radar signals much more than ice. But the crystals remain the same size as before, which means that they will have a much larger effective area. As the melting crystals continue to fall downward, they continue to melt until the wet crystals become pure rain. Raindrops are smaller and also fall faster, so not only the size of the drops is reduced, but also their concentration. The reflectivity is therefore reduced below the bright band. The presence of a bright band is an indicator that precipitation is stratiform, since strong convective currents in active showers and thunderstorms destroy the horizontal stratification, which is however necessary for the formation of the bright band.

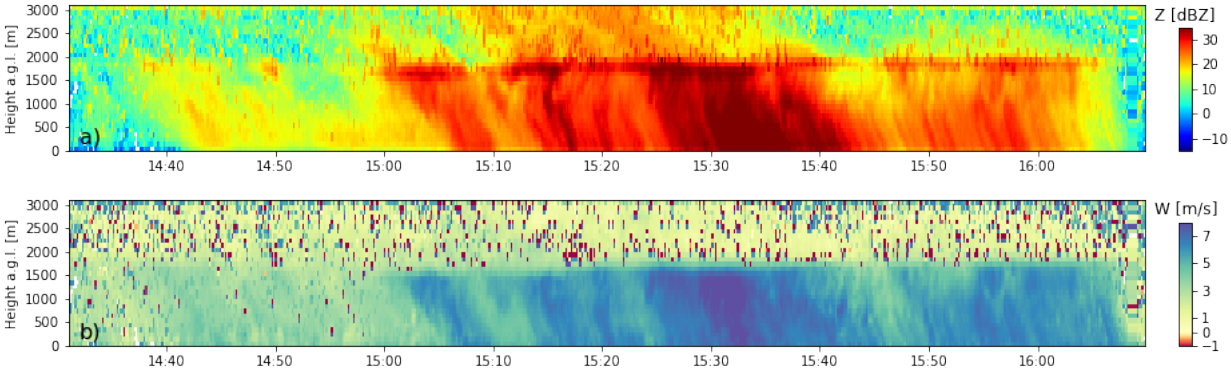

Figure 36. Rain event from 17 May 2008, in (**a**) the bright band is clearly visible as a continuously increased reflectivity at a height of about 2 km. In (**b**), a strong increase in velocity is recognisable at the height of the bright band, which can be attributed to the higher fall velocity of liquid precipitation compared to the fall velocity of ice crystals.

Complete Events

Figures 37 and 38 display the complete precipitation parameters measured by the MRR for the virga precipitation events of 8 April 2008 and 17 March 2013. In comparison to the shorter segments of the events shown in sections 7.4 and 7.5, no masks were applied to these figures.

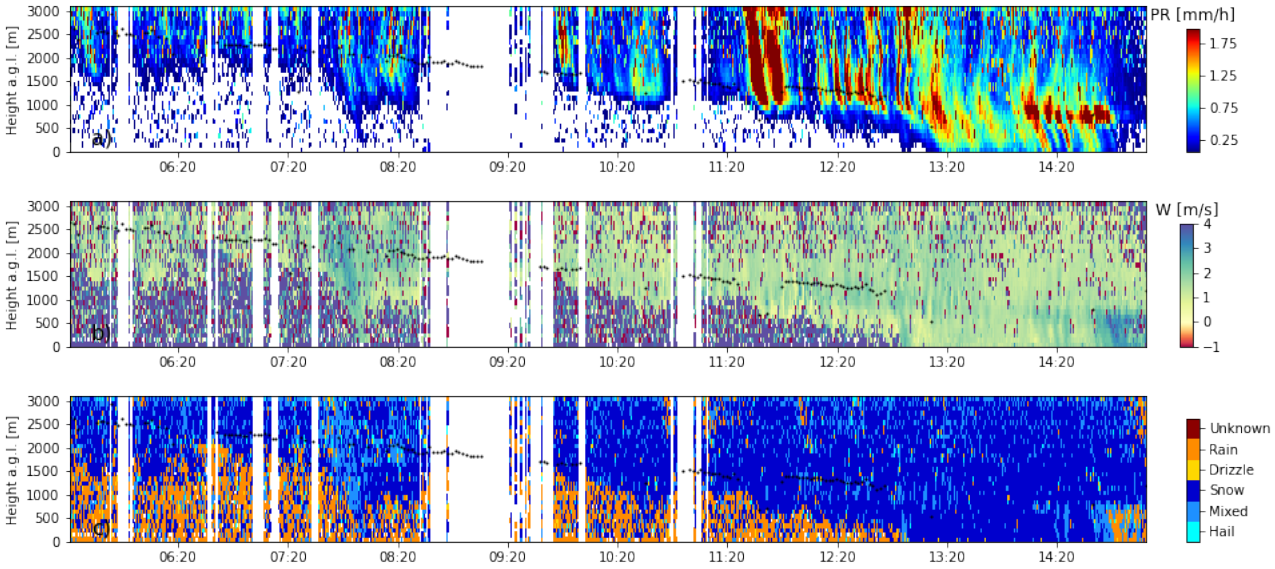

Figure 37. Complete virga event that occurred on 8 April 2008. The plots are all derived from MRR measurements using the data processing of Garcia-Benadi et al [6]. (**a**) time-height plot of the precipitation rate. (**b**) time-height plot of the characteristic fall velocity. (**c**) time-height plot of the precipitation type. The cloud base detected by the ceilometer is highlighted by black dots.

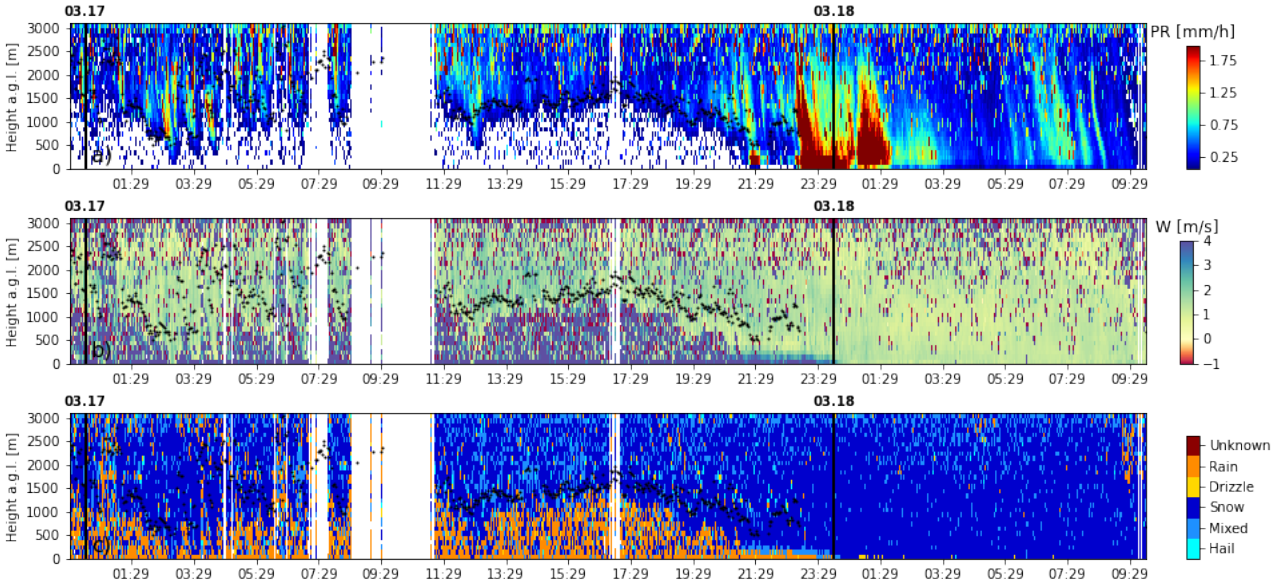

Figure 38. Complete virga event that occurred on 8 April 2008. The plots are all derived from MRR measurements using the data processing of Garcia-Benadi et al [6]. (**a**) time-height plot of the precipitation rate. (**b**) time-height plot of the characteristic fall velocity. (**c**) time-height plot of the precipitation type. The cloud base detected by the ceilometer is highlighted by black dots.

Additional virga precipitation events

Two additional virga precipitation events are presented in this section. However, these were not investigated further because they are both relatively short compared to those presented in the main work. The short duration makes the comparison with the reanalysis data from ERA5 difficult, as these have a temporal resolution of one hour, which is why short-term changes are not apparent.

Virga precipitation of 14 August 2008

The analysis of the event (see Fig. 39) starts on 19:33 and ends on 19:48 UTC. The event is quite short with a weak reflectivity of maximally 25 dBz. During the entire duration, a cloud layer was measured by the ceilometer, at an altitude of about 1 km. As a result of the rather weak reflectivity, it is not surprising that fairly low precipitation intensities of mostly less than 1.5 mm/h were observed. Between 19:36 and 19:40 UTC, a faint bright band can be seen at about 2.3 km height in the reflectivity, indicating a stratiform event. In the characteristic fall

velocity, the bright band is clearly visible, while the fall velocities above it fluctuate around 2 m/s, the fall velocities below it double up to 4 m/s. The bright band can also be seen quite clearly in the precipitation type classification, above a height of 2.5 km the precipitation is predominantly in the form of ice crystals, at the height of the bright band the precipitation melts and a mix of snow and rain forms, below this the precipitation is present in the form of rain, as one would also expect at this season.

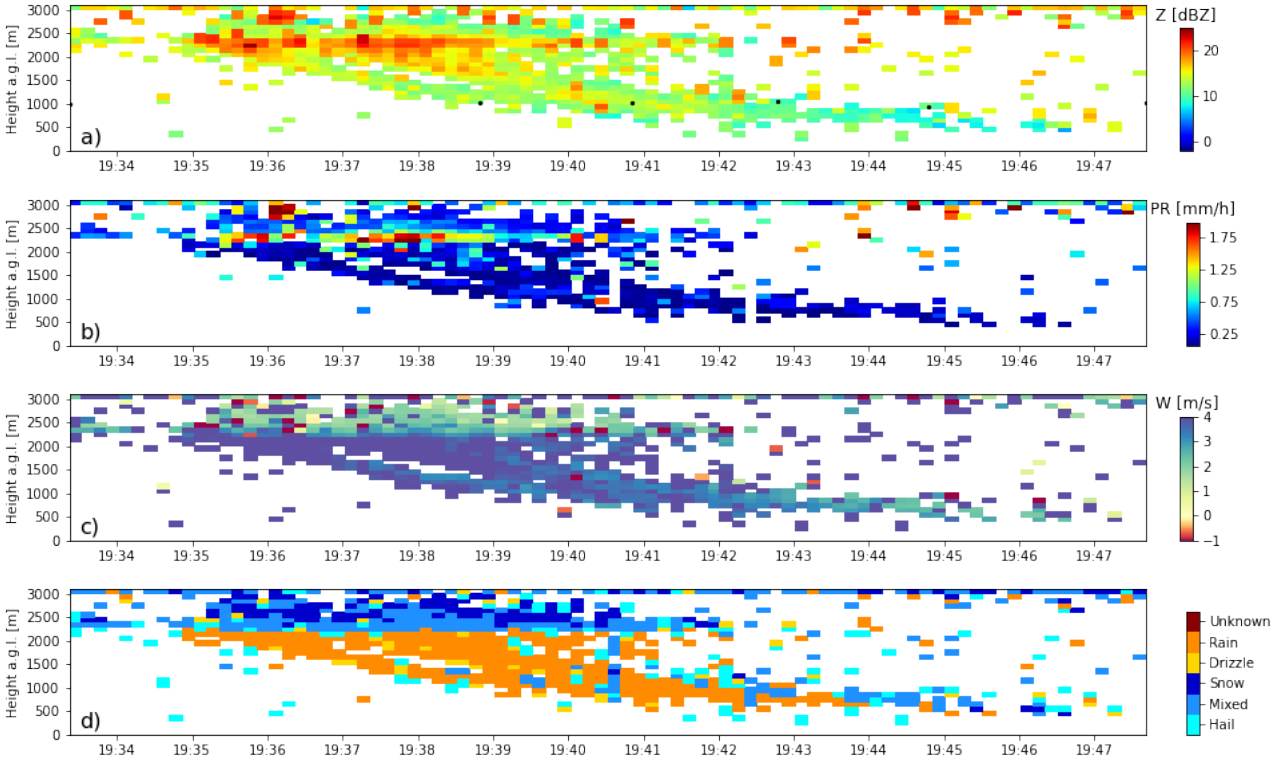

Figure 39. Case study of a precipitation event that occurred on 14 August 2008. The plots are all derived from MRR measurements using the data processing of Garcia-Benadi et al [6]. (**a**) time-height plot of the reflectivity. (**b**) time-height plot of the precipitation rate. (**c**) time-height plot of the characteristic fall velocity. (**d**) time-height plot of the precipitation type. The cloud base detected by the ceilometer is highlighted by black dots.

Observing the longer time series (Fig. 40), it is seen that the selected event is a pre-precipitation virga. Thereafter (around 20:15UTC), moderate to heavy precipitation begins, which lasts for at least 6 hours. The continuous bright band at a height between 2 and 2.3 km indicates that the precipitation is stratiform

throughout. Towards the end (starts at about 2:24UTC) there is a phase of very weak precipitation lasting about an hour, which however is not virga.

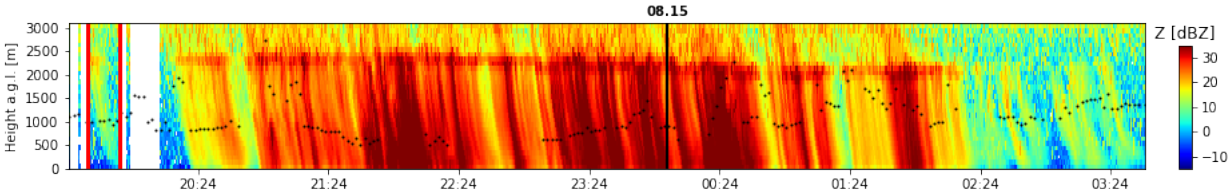

Figure 40. Radar reflectivity from 19:24 UTC on 14 August 2008 until 03:40 UTC on 15 August 2008. The red lines mark the selected virga event, see Fig. 39. The empty spaces represent missing raw data due to the conditional recording.

Observing the time series of the ERA5 data over Bern Fig. 41, a wind shear in the northward wind component (**c**) can be noticed during the virga precipitation phase. However, the wind shear is not only present during the virga phase but throughout the entire precipitation period, albeit slightly less pronounced. In the vertical velocity component (**b**), also an updraft can be seen during the virga phase at an altitude between 500 - 3000 m above the ground, but it is rather weak.

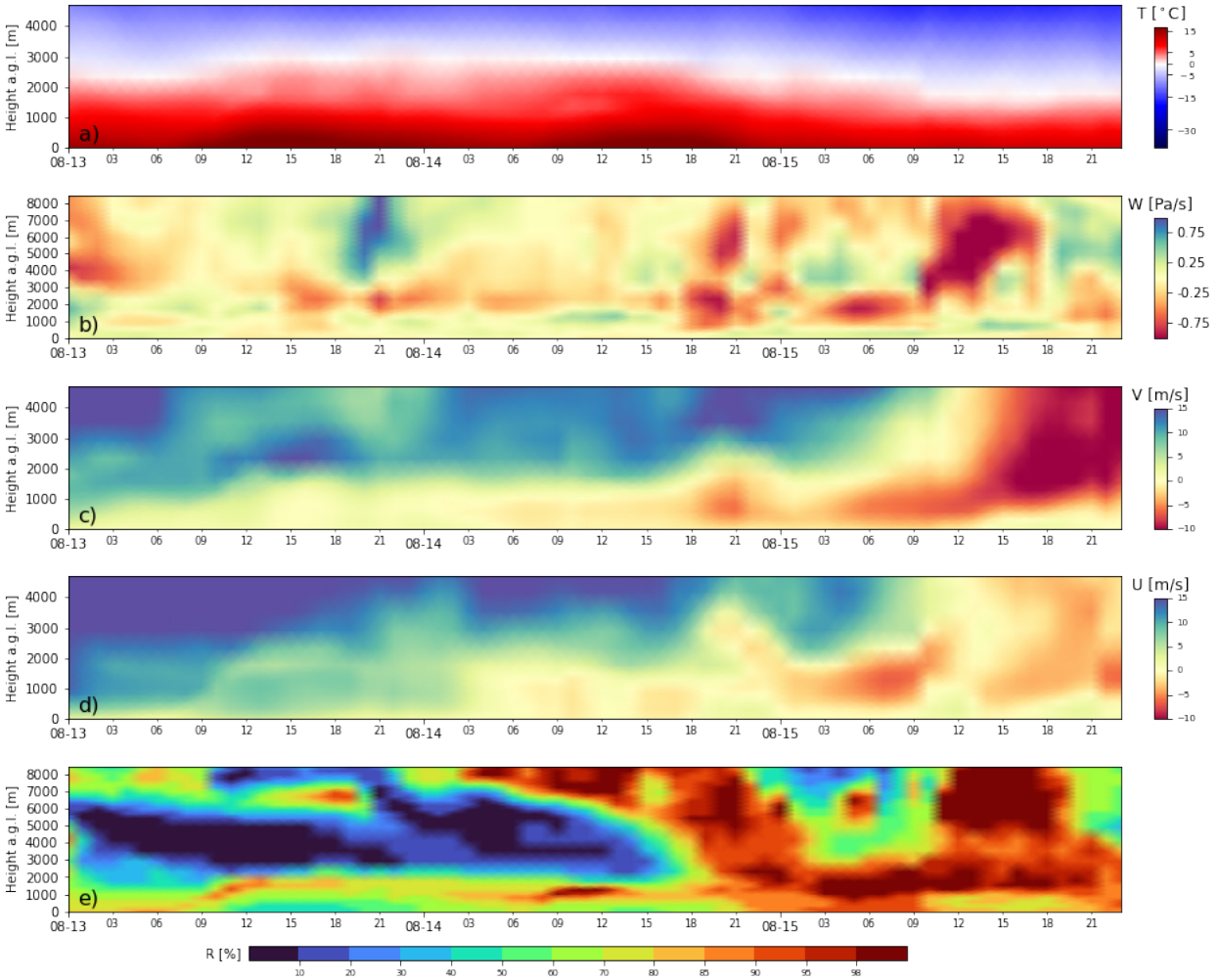

Figure 41. ERA5 data at grid point close to Bern from 13 August 2008 up to and including 15 August 2008 with a temporal resolution of one hour. (**a**) time-height plot of the temperature. (**b**) time-height plot of the vertical velocity. (**c**) time-height plot of northward component of the wind. (**d**) time-height plot of the eastward component of the wind. (**e**) time-height plot of the relative humidity.

Virga precipitation of 28 October 2008

The analysis of the event (see Fig. 42) starts on 08:13 and ends on 09:28 UTC. The reflectivity is rather low until about 08:48 UTC, at that time the activity increases, which then also leads to precipitation that reaches the ground at about 09:22 UTC. The ceilometer measured a cloud layer until 08:48 UTC, at a height between 1.5 and 1.6 km, afterwards the ceilometer could no longer determine a cloud layer, presumably due to the increasing precipitation. The precipitation rates are also rather low during the virga period, mostly below 1 mm/h, until the time of increased activity in which the precipitation rates exceed 4 mm/h. Based on the classification, precipitation can be assumed to be snow, which is also consistent with the values of the characteristic fall velocity, which are mostly in a range between 1 and 2 m/s.

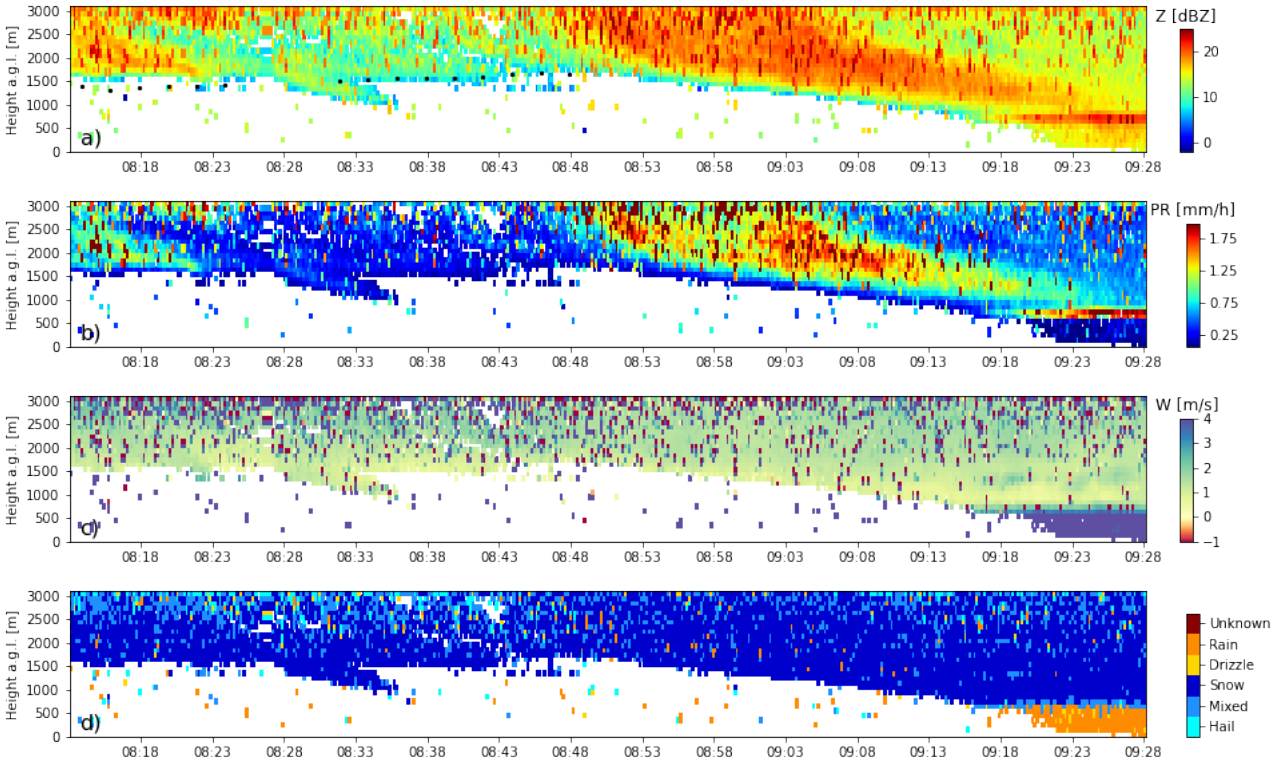

Figure 42. Case study of a precipitation event that occurred on 28 October 2008. The plots are all derived from MRR measurements using the data processing of Garcia-Benadi et al [6]. (**a**) time-height plot of the reflectivity. (**b**) time-height plot of the precipitation rate. (**c**) time-height plot of the characteristic fall velocity. (**d**) time-height plot of the precipitation type. The cloud base detected by the ceilometer is highlighted by black dots.

In the larger time section (Fig. 43) it can be seen that there was ground precipitation both before and after the selected virga event. The precipitation before the Virga event is rather inhomogeneous, with alternating short phases of precipitation, but a bright band, albeit weak, is always visible. Between 04:00 UTC and 06:00 UTC the bright band starts to decrease from a height of 1.5 km to 1.1 km, in the next precipitation event starting at 09:30 UTC it is then at a height of slightly above 0.5 km, from which it can be concluded that the temperature has decreased during this period. Between these two ground precipitation events, the virga phase occurs, with a data gap at 07:00 UTC and precipitation measured near the ground at around 07:30, although very weak.

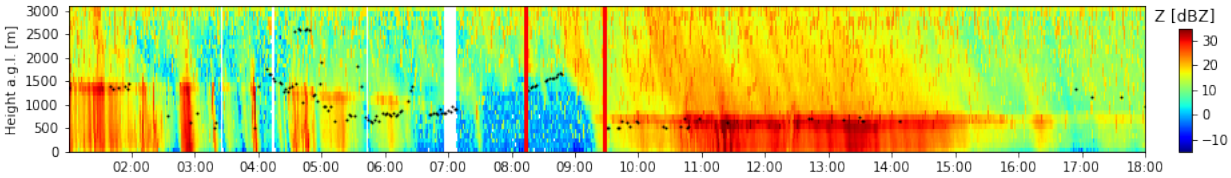

Figure 43. Radar reflectivity of 28 October 2008 from 01:00 to 18:00 UTC. The red lines mark the selected virga event, see Fig. 42. The empty spaces represent missing raw data due to the conditional recording.

In the time series of the ERA5 data over Bern Fig. 44 we can see that a weak wind shear is visible in the northward wind component (**c**), which was present before, during and after the virga phase. However, if we also look at the relative humidity profile (**e**), we see that the air was saturated at all altitudes, which means that saturated air was also carried over Bern near the ground.

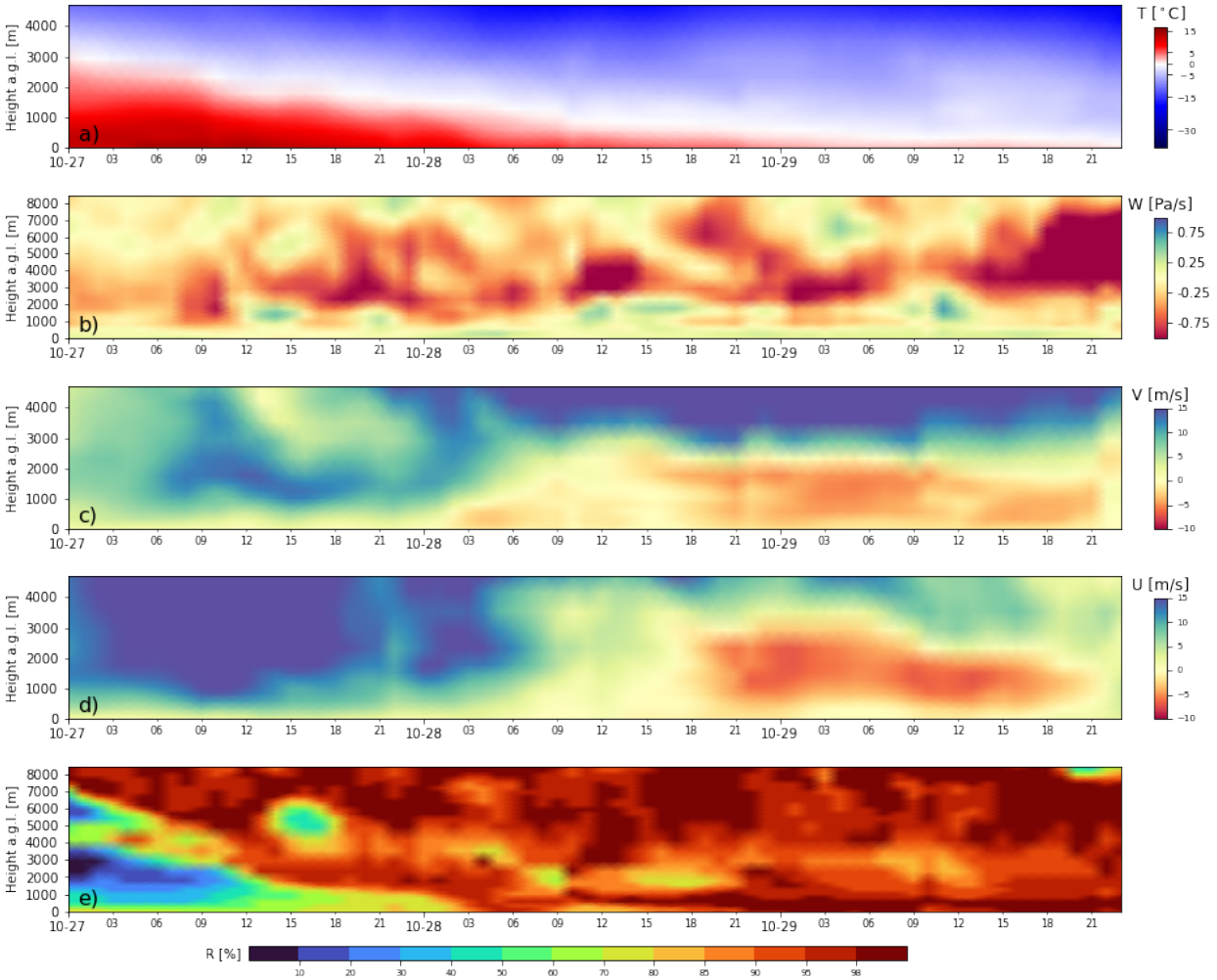

Figure 44. ERA5 data at grid point close to Bern from 27 October 2008 up to and including 29 October 2008 with a temporal resolution of one hour. (**a**) time-height plot of the temperature. (**b**) time-height plot of the vertical velocity. (**c**) time-height plot of northward component of the wind. (**d**) time-height plot of the eastward component of the wind. (**e**) time-height plot of the relative humidity.

Bibliography

[1] Swiss Severe Weather Database (SSWD). *Sturmarchiv Schweiz - Extremereignisse 2009*. URL: http://sturmarchiv.ch/index.php?title=Extremereignisse_2009.

[2] D. Atlas, R. C. Srivastava, and R. S. Sekhon. *Doppler radar characteristics of precipitation at vertical incidence*. Feb. 1973. DOI: 10.1029/RG011i001p00001.

[3] Joo Wan Cha et al. "Comparison of the bright band characteristics measured by Micro Rain Radar (MRR) at a mountain and a coastal site in South Korea". In: vol. 26. Springer, Mar. 2009, pp. 211–221. DOI: 10.1007/s00376-009-0211-0.

[4] G Foote and P Du Toit. "Terminal Velocity of Raindrops Aloft". In: *Journal of Applied Meteorology and Climatology* (1969). DOI: https://doi.org/10.1175/1520-0450(1969)008<0249:TVORA>2.0.CO;2.

[5] Shoichiro Fukao and Kyosuke Hamazu. *Radar for Meteorological and Atmospheric Observations*. Springer Japan, 2014. ISBN: 978-4-431-54740-2. DOI: 10.1007/978-4-431-54334-3.

[6] Albert Garcia-Benadi et al. "Precipitation type classification of micro rain radar data using an improved doppler spectral processing methodology". In: *Remote Sensing* 12 (24 Dec. 2020), pp. 1–23. ISSN: 20724292. DOI: 10.3390/rs12244113.

[7] R Gunn and G Kinzer. "THE TERMINAL VELOCITY OF FALL FOR WATER DROPLETS IN STAGNANT AIR". In: *Journal of the Atmospheric Sciences* (1949). DOI: https://doi.org/10.1175/1520-0469(1949)006<0243:TTVOFF>2.0.CO;2.

[8] Hans Hersbach et al. *ERA5 hourly data on pressure levels from 1979 to present*. DOI: 10.24381/cds.bd0915c6. (Visited on 10/11/2021).

[9] Hans Hersbach et al. *ERA5 hourly data on single levels from 1979 to present*. DOI: 10.24381/cds.adbb2d47. (Visited on 10/11/2021).

[10] Hans Hersbach et al. "The ERA5 global reanalysis". In: *Quarterly Journal of the Royal Meteorological Society* 146 (730 July 2020), pp. 1999–2049. DOI: 10.1002/QJ.3803.

[11] P Hildebrand and R Sekhon. "Objective Determination of the Noise Level in Doppler Spectra". In: *Journal of Applied Meteorology and Climatology* (Oct. 1974), pp. 808–811. DOI: https://doi.org/10.1175/1520-0450(1974)013<0808:ODOTNL>2.0.CO;2.

[12] Markus Imhof and Marc Choffet. *Ereignisanalyse Hagel 2009*. Interkantonaler Ruckversicherungsverband IRV, 2012.

[13] Nicolas Jullien et al. "Synoptic conditions and atmospheric moisture pathways associated with virga and precipitation over coastal Adelie Land in Antarctica". In: *Cryosphere* 14 (5 May 2020), pp. 1685–1702. ISSN: 19940424. DOI: 10.5194/TC-14-1685-2020.

[14] Stefan Kneifel et al. "Observation of snowfall with a low-power FM-CW K-band radar (Micro Rain Radar)". In: *Meteorology and Atmospheric Physics* 113 (1 June 2011), pp. 75–87. ISSN: 01777971. DOI: 10.1007/S00703-011-0142-Z/FIGURES/10.

[15] NOAA Air Resources Laboratory. *on-line READY web version of HYSPLIT*. URL: https://www.ready.noaa.gov/HYSPLIT_traj.php.

[16] Andreas Leuenberger. *Precipitation Measurements with Microwave Sensors*. 2009.

[17] M. Maahn and P. Kollias. "Improved Micro Rain Radar snow measurements using Doppler spectra post-processing". In: *Atmospheric Measurement Techniques* 5 (11 2012), pp. 2661–2673. ISSN: 18671381. DOI: 10.5194/amt-5-2661-2012.

[18] Sergey Y. Matrosov. "Modeling Backscatter Properties of Snowfall at Millimeter Wavelengths". In: *Journal of the Atmospheric Sciences* 64 (5 May 2007), pp. 1727–1736. ISSN: 1520-0469. DOI: 10.1175/JAS3904.1.

[19] METEK. *Micro Rain Radar - User Manual*. 2012. URL: http://www.metek.de.

[20] METEK. *MRR Physical Basics*. 2010. URL: http://www.metek.de.

[21] METEK. *MRR Tutorial*. 2017. URL: http://www.metek.de.

[22] SRF Meteo. *Wetterbericht Meteo SRF*. 2008. URL: https://www.srf.ch/meteo/wetterbericht/2008-04-07.

[23] SRF Meteo. *Wetterbericht Meteo SRF*. 2008. URL: https://www.srf.ch/meteo/wetterbericht/2008-04-08.

[24] SRF Meteo. *Wetterbericht Meteo SRF*. 2013. URL: https://www.srf.ch/meteo/wetterbericht/2013-03-16.

[25] SRF Meteo. *Wetterbericht Meteo SRF*. 2013. URL: https://www.srf.ch/meteo/wetterbericht/2013-03-17.

[26] MeteoSchweiz. "Annalen 2008". In: (2008). ISSN: 0080-7338.

[27] MeteoSchweiz. *Schneefall im Frühling*. URL: https://www.meteoschweiz.admin.ch/home/klima/klima-der-schweiz/altweibersommer-eisheilige-und-andere-spezialitaeten/schneefall-im-fruehling.html.

[28] Gerhard Peters, Bernd Fischer, and Marco Clemens. "Rain attenuation of radar echoes considering finite-range resolution and using drop size distributions". In: *Journal of Atmospheric and Oceanic Technology* 27 (5 May 2010), pp. 829–842. ISSN: 07390572. DOI: 10.1175/2009JTECHA1342.1.

[29] Glenn Rolph, Ariel Stein, and Barbara Stunder. "Real-time Environmental Applications and Display sYstem: READY". In: *Environmental Modelling and Software* 95 (Sept. 2017), pp. 210–228. ISSN: 1364-8152. DOI: 10.1016/J.ENVSOFT.2017.06.025.

[30] A. F. Stein et al. "NOAA HYSPLIT Atmospheric Transport and Dispersion Modeling System". In: *Bulletin of the American Meteorological Society* 96 (12 Dec. 2015), pp. 2059–2077. ISSN: 0003-0007. DOI: 10.1175/BAMS-D-14-00110.1.

[31] Fawwaz T. Ulaby et al. *Microwave Radar and Radiometric remote Sensing*. The University of Michigan Press, 2014. ISBN: 978-0-472-11935-6.

[32] *University of Bern Microwave Group Data Storage*. URL: https://dataportal.mw.iap.unibe.ch/storage/.

[33] Vaisala. *CEILOMETER CT25K User Guide*. 1999. URL: https://www.vaisala.com.

[34] Malte Vöge and Matthias Hort. "Installation of a doppler radar monitoring system at Merapi Volcano, Indonesia". In: *IEEE Transactions on Geoscience and Remote Sensing* 47 (1 Jan. 2009), pp. 251–271. ISSN: 01962892. DOI: 10.1109/TGRS.2008.2002693.

[35] Hong Wang, Hengchi Lei, and Jiefan Yang. "Microphysical processes of a stratiform precipitation event over eastern China: analysis using micro rain radar data". In: *Advances in Atmospheric Sciences* 34 (12 Dec. 2017), pp. 1472–1482. ISSN: 02561530. DOI: 10.1007/s00376-017-7005-6.

[36] Yu Wang, Yalei You, and Mark Kulie. "Global Virga Precipitation Distribution Derived From Three Spaceborne Radars and Its Contribution to the False Radiometer Precipitation Detection". In: *Geophysical Research Letters* 45 (9 May 2018), pp. 4446–4455. DOI: 10.1029/2018GL077891.

[37] James W. Wilson and Roger M. Wakimoto. "The Discovery of the Downburst: T. T. Fujitas Contribution". In: *Bulletin of the American Meteorological Society* 82 (1 Jan. 2001). ISSN: 0003-0007. DOI: 10.1175/1520-0477(2001)082<0049:TDOTDT>2.3.CO;2.